Fluid mixing as the cause of sulphide precipitation at Albrunpass, Binn Valley, Central Alps

Autor(en): **Klemm, L. / Pettke, T. / Graeser, S.**

Objekttyp: **Article**

Zeitschrift: **Schweizerische mineralogische und petrographische Mitteilungen = Bulletin suisse de minéralogie et pétrographie**

Band (Jahr): **84 (2004)**

Heft 1-2: **Geodynamics and Ore Deposit Evolution of the Alpine-Carpathian-Balkan-Dinaride Orogenic System**

PDF erstellt am: **24.04.2024**

Persistenter Link: https://doi.org/10.5169/seals-63746

Schweizerische Mineralogische und Petrographische Mitteilungen 84, 189–212, 2004

Fluid mixing as the cause of sulphide precipitation at Albrunpass, Binn Valley, Central Alps

L. Klemm[1,2], T. Pettke[1], S. Graeser[2], J. Mullis[2] and *K. Kouzmanov[1]*

Abstract

Alpine, late metamorphic lead ± zinc occurrences, albeit generally sub-economic, are widespread in Triassic metasedimentary rocks of the central Alps including the Binn Valley region in Switzerland. The PVTX properties of the mineralising fluid were determined by microthermometry, Raman spectroscopy and LA-ICPMS. It is demonstrated that low-salinity CO_2-dominated fluid inclusions (1–2 wt% $NaCl_{equiv}$) can be analysed reliably by LA-ICPMS. The data reveal an evolutionary sequence of fluid generations that monitors incursion of a metal-charged brine (~31 wt% $NaCl_{equiv}$; Pb ~13'000 µg/g (= 63 µmol/g); Zn ~6500 µg/g (= 99 µmol/g)) and progressive mixing of it in a pre-existing, low-salinity (1–2 wt% $NaCl_{equiv}$), CO_2-dominated aqueous fluid. Simple modelling suggests that the increase in activity of reduced sulphur in the mixture, provided by the aqueous CO_2-rich fluid, was the principal trigger of galena deposition. Sphalerite was virtually never saturated during fluid evolution, owing to the much higher solubility of ZnS relative to PbS at the specific temperature (~270 °C), pH (<4) and activity of reduced sulphur (~10^{-3} mol/kg). High concentrations of Ba, Ca and Sr imply that the brine was derived from, or interacted with, Triassic evaporites. Likewise, the high metal concentrations suggest fluid interaction with a „Bleiberg-type" Pb–Zn enrichment. The small but high-grade Pb–Zn deposits scattered throughout Triassic lithologies in the Alps may thus commonly represent rather local remobilisation of Triassic syngenetic „Bleiberg-type" base metal occurrences late in the tectono-metamorphic evolution of the Alps.

Keywords: Hydrothermal fluid evolution, mineralisation, laser-ablation ICP-MS, Mississippi Valley Type ore deposit.

Introduction

One of the world's most important sources of Pb, Zn and some of the Ag are Mississippi-Valley-Type (MVT) ore deposits. They form by basin-scale migration of sedimentary brines, from which the ore metals were commonly deposited in carbonate rocks, often during multiple events (e.g., Leach and Sangster, 1993). Other genetic types of base metal deposits, economically less significant on a global scale, include those linked to metamorphism of the host rock units (e.g., Mt. Isa, Heinrich, 2000). Triassic rocks of the European Alps commonly host such deposits, too, albeit economically insignificant except at a few localities such as Bleiberg, Austria (e.g., Köppel and Schroll, 1985; Schroll, 1996). Nevertheless, smaller deposits and occurrences scattered across the Alps were mined in the past as documented by old adits and some historic records.

Among such localities in Switzerland, the region of the Binn Valley (Binntal in German) has attracted most research interest (e.g., Graeser, 1965; Knill, 1996; Krzemnicki, 1992; Hofmann, 1994; Hofmann and Knill, 1996), thanks to the Pb–Zn–As–Tl–Ba deposit at the Lengenbach site, which is world-famous for Pb–Zn–As–Tl sulphosalt minerals. The various base metal occurrences, mostly hosted by Triassic metasediments in the region are very likely genetically linked. The genesis of these occurrences has remained controversial, however. In his pioneering work, Graeser (1965 and 1976) proposed that the formation of the deposits in the Binn Valley results from metamorphic remobilisation of two distinct pre-Alpine metal occurrences: Pb–Zn–Ba occurrences hosted in Triassic rocks and Cu–As–Sb enrichments observed in basement rocks of the Monte Leone nappe. Hoefs and Graeser (1968) proposed a sedimentary origin for the pre-Alpine occurrence based on S isotopes. Krzemnicki (1992) studied some of the Cu–As anomalies in the Monte Leone nappe and found evidence for high mobility of Cu and As along faults during Alpine metamorphism. However, Knill (1996) concluded from Sr, S, C and O isotope data that the Lengenbach deposit is the result of a pre-Alpine, sediment-hosted Mesozoic sulphide mineralisation,

[1] Institute of Isotope Geochemistry and Mineral Resources, ETH-Zentrum, CH-8092 Zürich, Switzerland. <klemm@erdw.ethz.ch>
[2] Institute of Mineralogy, University of Basel, Bernoullistr. 30, CH-4056 Basel, Switzerland.

0036-7699/04/0084/189

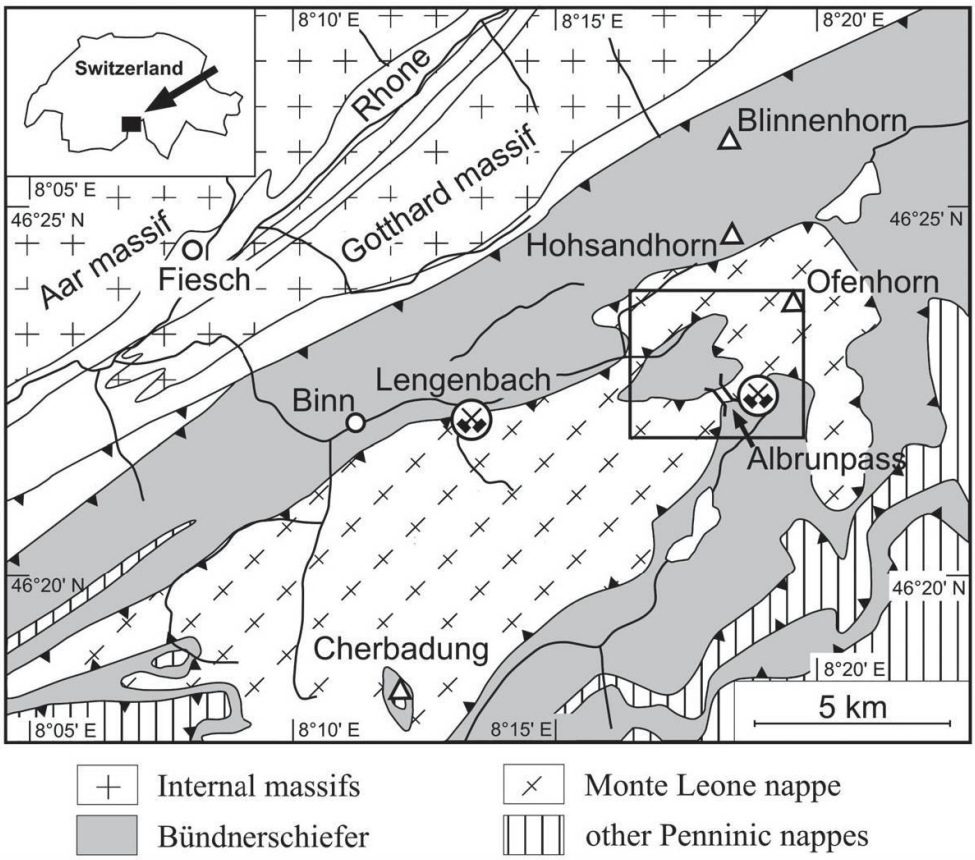

Fig. 1 Tectonic map of the larger Binn Valley area, Switzerland/Italy, where numerous base metal occurrences are associated with Triassic lithologies of the Monte Leone nappe (simplified after Spicher, 1988). The box marks the enlargement shown in Fig. 2.

which was overprinted by regional Alpine metamorphism. Sr isotopes show no evidence for significant input from outside the Triassic sequence. Sulphide inclusions in quartz from the Lengenbach deposit have been interpreted as the remains of a sulphide melt present during peak metamorphic conditions (Hofmann, 1994; Hofmann and Knill, 1996). In summary, the genesis of the Lengenbach Pb–Zn–As–Tl–Ba deposit is now believed to be the product of an Alpine metamorphic remobilisation of a Triassic sedimentary exhalative sulphide deposit (Knill, 1996; Hofmann and Knill, 1996; Heinrich et al., 2000).

The aim of this study is to better constrain the characteristics of the hydrothermal fluid from which the base metal occurrences in the Triassic metasediments of the region of the Binn Valley formed. Detailed field observations are coupled with mineralogical and mineral-chemical data and careful fluid inclusion work. Standard petrographic and microthermometric procedures form the basis for a Laser-Ablation Inductively-Coupled-Plasma Mass-Spectrometry (LA-ICPMS) study of the chemical evolution of the hydrothermal fluid. A relatively small Pb occurrence near the Swiss-Italian border at Albrunpass was selected because of its clear field relations and structural simplicity. The conclusions drawn here are considered valid for other Triassic metasediment-hosted base metal deposit in the region and possibly elsewhere in the Alps.

Geologic setting

A small Pb occurrence, mined for Pb and Ag in 1576 (Archivio di Stato di Milano, 1576) is situated on the Italian side of the Albrunpass (Figs. 1,2), which separates the upper Binn Valley (Switzerland) from the Alpe Devero in the upper Formazza Valley (Italy). The occurrence is hosted by Triassic metasediments that are autochthonous on ortho- and paragneiss units of the Penninic Monte Leone nappe (Fig. 2). Breccias and rauhwackes sometimes line the contact between Triassic rocks and the Monte Leone nappe. Cretaceous calcschists ("Bündnerschiefer") of the Feldbach zone discordantly overlie the Monte Leone nappe. In the area of the Binn Valley the stratigraphy is overturned, so that the sequence observed in the field is from bottom to top: Cretaceous calcschists followed by Triassic metasediments followed by basement gneisses of the Monte Leone nappe. Figure 2 shows a detailed geological map of the mineralised area.

The Monte Leone nappe consists of pre-Mesozoic ortho- and paragneisses with occasionally in-

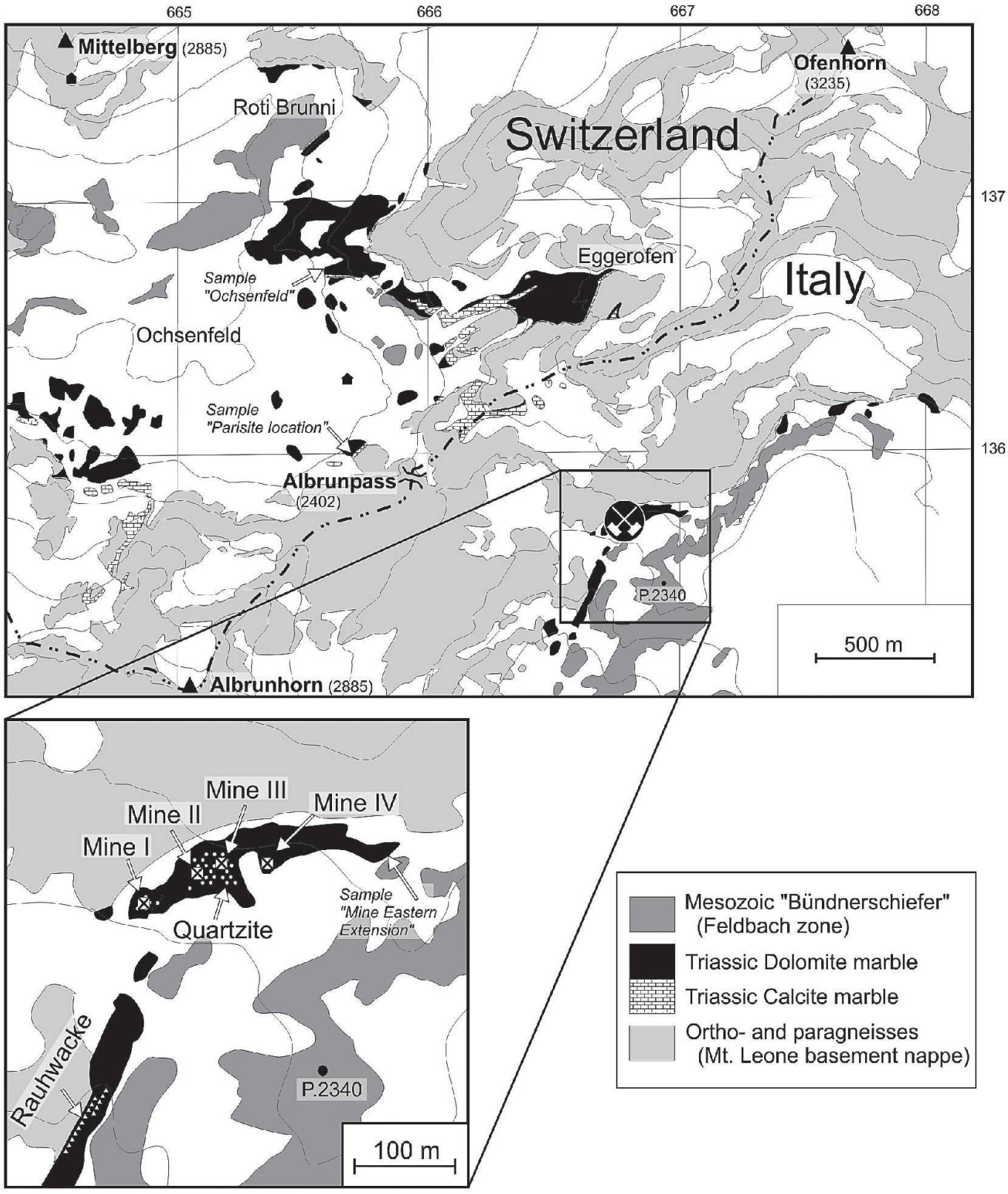

Fig. 2 Lithological outcrop map of the study area around Albrunpass, representing the box in Fig. 1. Cretaceous Bündnerschiefer overlie Triassic dolomite marble and calcite marble, which represent the sedimentary cover of the pre-Mesozoic basement rocks of the Monte Leone nappe. The gneisses of the Monte Leone nappe and the Bündnerschiefer of the Feldbach zone are lithologically variable, but undifferentiated here. Breccias, rauhwackes and quartzites are only resolved in the detail map.

tercalated amphibolite lenses (Bader, 1934). At the locality "Ochsenfeld", Bündnerschiefer crop out in a small tectonic window. Bündnerschiefer also occur on the Italian side of the Albrunpass. These rocks consist mainly of quartz, white and dark micas with variable amounts of garnet, kyanite and staurolite. Carbonates are only subordinate. The gneisses of the Monte Leone nappe as

Table 1 Data from microthermometry (upper part of the table) and the results of the calculations (lower part of the table).

FI generation	Inclusion type (daughter minerals)	N	Vol% bubble	$T_{m\ CO2}$ (°C)	$T_{m\ H2O}$ (°C)	$T_{m\ Clath.}$ (°C)	$T_{h\ CO2}$ (°C)	$T_{m\ Salt1}$ (°C)	$T_{m\ (halite)}$ (°C)	$T_{h\ H2O}$ (°C)	$T_{h\ total}$ (°C)	$NaCl_{equiv.}$ (wt%)
A	CO_2, H_2O (2 op)	36	60–80	–56.5 (–56.7; –56.2)	n.o.	9.5 (9.2; 9.9)	21.8 V (13.0; 29.0)	–	–	–	n.o.	1 +/– 0.42
B	H_2O, (hl, cc, Ba)	29	10	–	n.o.	–	–	117 (107; 125)	188 (164; 201)	239 L (212; 272)	239 (212; 272)	31 +/– 0.47
BC1	H_2O, CO_2, (hl, cc, Ba)	2	30	–56.6 (–56.6; –56.5)	n.o.	–10 (inferred)	30 C (29.5; 30.3)	72	107 (103; 113)	n.o.	n.o.	25 +/– 1.24
BC2	CO_2, H_2O	3	80–90	–56.3 (–56.5; –56.2)	n.o.	6.5 (6.1; 7.0)	29.9 V (29.8; 30.0)	–	–	–	n.o.	6.4 +/– 1.12
C	CO_2, H_2O	39	80–90	–56.2 (–56.1; –56.4)	n.o.	9.07 (8.6; 9.8)	28.6 V (26.0; 30.5)	–	–	–	274 L (268; 283)	1.9 +/– 0.7
D	H_2O	12	5	–	–0.8 (–0.9; –0.6)	–	–	–	–	159 L (152; 172)	159 L (152; 172)	1.4 +/– 0.15

FI generation	CO_2 dissolved (wt%)	ρ H_2O (g/cm³)	ρ CO_2 (g/cm³)	ρ inclusion (g/cm³)	H_2O +) (Mol%)	CO_2 +) (Mol%)	Na *) (Mol%)	K *) (Mol%)	Ca *) (Mol%)	Ba *) (Mol%)	Zn *) (Mol%)	Pb *) (Mol%)
A	3.35	1	0.75	0.8	44	55	0.7	0.06	0.1	0.002	0.002	0.0001
B	0	1.16 x)	–	1.16	90	(traces)	6.0	0.7	2.1	1.3	0.2	0.1
BC1	0.75	1.19	0.6	1.01	80	10	4.8	0.5	2.8	1.4	0.2	0.1
BC2	2.60	1.04	0.6	0.69	48	49	1.9	0.5	0.9	0.24	0.08	0.04
C	3.25	1.01	0.65	0.69	29	70	1.1	0.1	0.3	0.01	0.004	0.001
D	0	1.01	–	1.01	99.6	0	0.4	n.a.	n.a.	n.a.	n.a.	n.a.

Numbers in brackets are minimum and maximum values
N—Number of inclusions
Vol% bubble—Volume fraction of the H_2O vapour bubble or CO_2 liquid+vapour
$T_{h\ CO2}$—Total homogenisation temperature of the CO_2; V—dew point transition, C = critical homogenisation
$T_{m\ Clath}$—Final melting temperature of the CO_2-clathrate
$T_{h\ H2O}$—Total homogenisation temperature of the H_2O; L—bubble point transition
$T_{m\ H2O}$—Final melting temperature of the H_2O (ice)
$T_{m\ Salt1}$—Dissolution temperature of the unknown Ba-bearing daughter crystal
$T_{h\ total}$—Homogenisation temperature of the bulk inclusion; L—bubble point transition
$NaCl_{equiv.}$ (wt%)—Weight percent NaCl-equivalent (calculated using the equations after Bodnar and Vityk (1994) for final dissolution of halite and after Diamond (1992) for final melting of clathrate)
op—opaque daughter mineral
hl—halite
cc—calcite
Ba—unidentified Ba-bearing daugther mineral
CO_2 dissolved—Amount of CO_2 dissolved in the H_2O-phase (after Mullis et al., 1994)
ρ $_{H2O}$—Density of vapour saturated NaCl solutions (after Potter et al., 1977)
x) —After Driesner et al. (2003)
ρ $_{CO2}$—Density of the CO_2-phase (after Angus et al., 1973)
ρ $_{inclusion}$—Bulk density of the inclusion using the equations of Mullis et al. (1994)
+)—Average molar fractions calculated using the equations of Mullis et al. (1994)
*)—Average molar fractions calculated using equations after Mullis et al. (1994) taking into account the data from LA-ICPMS shown in Table 2
n.o.—Not observed
n.a.—Not analysed

well as the Bündnerschiefer of the Feldbach zone are very variable in composition and texture. These variations were not resolved in detail for this study. More detailed petrographic descriptions of these units and their tectonic relations can be found in Bader (1934), Lüthy (1965) and Leu (1986). Regional Alpine metamorphism reached amphibolite facies conditions of 550 °C at 6.5 kbar (Todd and Engi, 1997).

The Triassic sequence of metasediments (mainly dolomite and calcite marbles and quartzite) in the region of the Binn Valley is interpreted as the overturned sedimentary cover of the Monte Leone nappe (Bianchi, 1998). It is lithologically variable, strongly deformed and folded, and ranges in thickness from less than a meter to a few hundred meters. The dolomite marbles are volumetrically dominant, usually sugar-grained (average grain size below 1 mm) and bright white to dark grey in colour due to variable contents of organic matter. A very distinct layering is characteristic, with some layers containing high amounts of phlogopite and/or tourmaline. Quartz–calcite–tremolite nodules are common. The calcite marbles are much thinner than the dolomite-marbles. Calcite-marbles are usually coarse-grained (1–2 mm grain size) and are brownish to yellowish in colour. Occasionally they contain large amounts of phlogopite crystals, sometimes exceeding 10 cm in diameter. Quartzite occurs in elongated lenses enclosed in dolomite-marbles and, interestingly, such lenses were observed only in places where the Triassic sequence is thinned to less than 10 m. These lenses are several meters long, and the appearance of the quartzite is similar to that of the dolomite marble. Quartzite contains minor carbonate, and the quartz grains show a strong undulous extinction and dynamic recrystallisation. In the field it cannot be resolved whether the quartzite is a metasandstone or the product of a pre- to syn-metamorphic hydrothermal alteration event. Quartzite is the only rock that hosts significant base metal occurrences near the Albrunpass. Minor clast-supported breccias contain clasts (<2 cm) of dolomite marble that are cemented by sugar-grained dolomite. Rauhwacke is rare and often crops out where the Triassic sequence was thinned to less than a few meters.

Analytical techniques

Mineral identification and chemical analyses were done by X-ray diffraction (XRD) and electron probe microanalysis (EPMA), respectively. Detailed fluid inclusion petrography provided information to select the assemblages (i.e., coevally trapped inclusions) that were investigated with conventional microthermometry, Raman spectroscopy and LA-ICPMS.

XRD: Powder XRD equipped with Bradley (90 mm) and Gandolfi (114.5 mm) cameras were used with 40 kV and 25 mA on an Fe Kα X-ray source to identify minerals and to determine their lattice parameters.

EPMA: The concentrations of S, Fe, Ni, Cu, Zn, As, Se, Ag, Cd, Sn, Sb, Te, and Pb in sulphides and sulphosalts were determined with a JEOL 8600 Superprobe electron microprobe at the MPI Basel using wavelength-dispersive techniques at 15 kV accelerating potential and 10 nA beam current for major and minor elements. These analyses were conducted with a slightly defocused beam (2–5 µm diameter) and peak counting times of 600 seconds for Fe, Ni, Cu, Zn, As, Se, Ag, Cd, Sn, Sb and Te and 20 seconds for Pb and S. Standardisation was mainly done on sulphides: S and Fe: Kα1 on pyrite; Ni: Kα1 on millerite; Cu: Kα1 on chalcopyrite; Zn: Kα1 on sphalerite; As: Lα1 on lordanite; Se: Lα1 on clausthalite; Ag and Sb: Lα1 on miargyrite; Cd: Lα1 on greenockite; Sn: Lα1 on ottemannite; Te: Lα1 on hessite; and Pb: Mα1 on clausthalite.

Microthermometry: Phase transitions in fluid inclusions were determined during heating, using a Linkam TS600 heating-freezing stage. Calibration of the system was performed on synthetic fluid inclusion standards (Syn Flinc®), and temperature readings are considered to be accurate to within ±0.5 at –60 °C, to within ±0.2 between 0 and 100 °C, and to within ±1 °C above 100 °C. Salinities were derived from final melting temperatures of clathrate for all low-salinity, CO_2-bearing inclusions after Diamond (1992) and from final melting temperatures of halite for all brines after Bodnar and Vityk (1994). The salinities of low-salinity, aqueous inclusions were calculated after Bodnar and Vityk (1994) using final melting of ice. The $NaCl_{equiv}$ values of the CO_2-bearing brine inclusions were calculated after Bodnar and Vityk (1994) neglecting the presence of CO_2, because the H_2O–CO_2–NaCl system is not well constrained for high salinities (Schmidt and Bodnar, 2000; Diamond, 1992).

Raman microspectrometry: Raman analyses were performed in the Laboratory of Raman spectrometry at ETH-Zürich using a LabRam (Dilor) spectrometer with a confocal entrance optics system. The system is equipped with an Olympus microscope and a CCD detector. The laser was focused using an Olympus 80× long working-distance objective (free working distance 180 µm, numerical aperture 0.75). Raman scattering was excited with a 632.8 nm HeNe laser

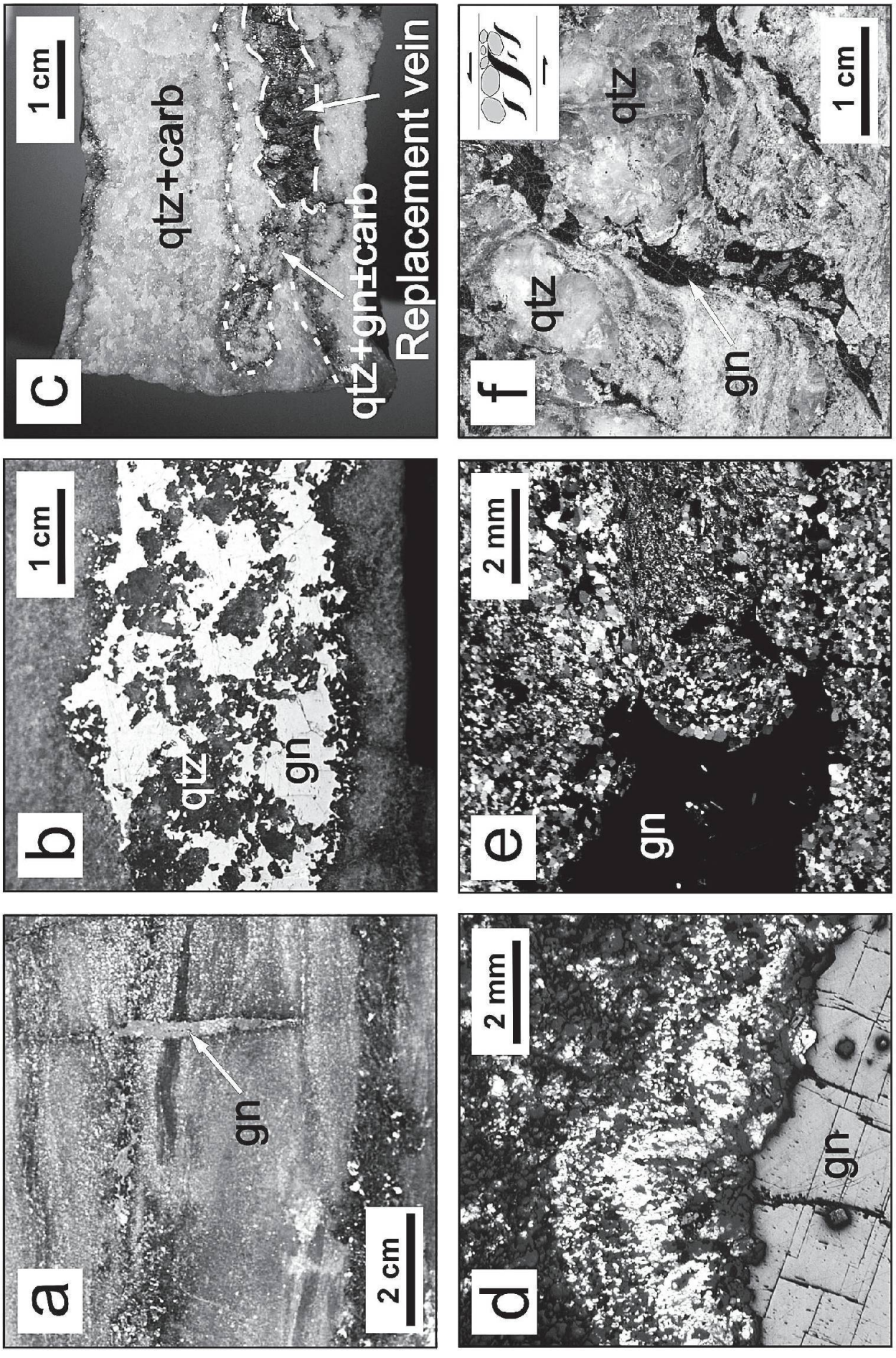

Fig. 3 Photographs of ore textures: (a) open space fissure filled with galena (gn); (b) replacement vein, consisting of quartz (qtz) and galena; (c) faint alteration envelope around a replacement vein; (d) microphotograph of a section though the same alteration envelope (combined reflected and transmitted light); (e) microphotograph of a thin section of a mineralised fold hinge (transmitting light, crossed nicols); (f) mineralised brittle shear zone, overprinting a former open space quartz-adularia fissure vein.

source at 20 mW laser output power. The spectral resolution was about 2 cm^{-1}. The spectrum of calcite as a solid phase in fluid inclusions was recorded in the range 200 to 1200 cm^{-1}. CO_2 and H_2S in the vapour phase of fluid inclusions are characterised by their strong responses at 1285 (CO_2) and 1388 cm^{-1} (CO_2), and 2611 cm^{-1}(H_2S), respectively. No attempt was made to quantify CO_2 and H_2S, however.

LA-ICPMS: Selected inclusions were finally analysed individually with LA-ICPMS, using the instrumental setup described in Günther et al. (1998) and Heinrich et al. (2003). Briefly, the setup uses a 193 nm ArF Excimer laser (Lambda Physik, Germany) combined with special beam energy homogenisation optics (Microlas, Germany) and linked with an Elan 6100 quadrupole ICP-MS instrument (Perkin Elmer, Canada). For controlled ablation of the quartz-hosted fluid inclusions, an output-energy of 130 mJ and a laser pulse frequency of 10 Hz was used. The design as an optical imaging system permits the use of different pit sizes (4–80 µm) at constant energy density on the sample, by adjusting an aperture in the laser beam path. The ablation process was monitored both on the sample and as real-time signal on a monitor to ensure best-possible control of the ablation process. For external standardisation the NIST glass standard SRM-610 was used, providing relative element concentrations for each sample. The concentration of Na in the fluid was then used as an internal standard to transform the relative element concentrations into absolute values. These Na concentrations were derived from the microthermometric NaCl equivalent values (see below) corrected for contributions of KCl, $CaCl_2$, $FeCl_2$, $MnCl_2$, $PbCl_2$, $ZnCl_2$ and $BaCl_2$. Details on each step of the quantification procedure are outlined in Heinrich et al. (2003). Limits of detection (LOD) were calculated for each element in each inclusion individually as three standard deviations of the background signal divided by its corresponding sensitivity (Longerich et al., 1996), except where stated otherwise.

Results

Observations on mineralised structures, mineralogy and compositional data for galena and fahlores, the chemical and structural characterisation of an unknown sulphide mineral are presented first, followed by fluid inclusion petrography and microthermometry, and fluid-chemical data obtained by LA-ICPMS.

Structural control

The occurrence of sulphides is spatially related to quartzite lenses, surrounded by sugar-grained dolomite marble (Fig. 2). The primary sulphides fill open-space fissure veins (Fig. 3a) of up to a few dm thickness and overgrow a classical Alpine-type fissure paragenesis (Stalder et al., 1973), comprised mainly of quartz, adularia, rutile, muscovite, pyrite and dolomite. The sulphides also occur as cm-sized replacement veins parallel to the host rock foliation (Fig. 3b), that have a silicified and completely decarbonatised halo of 2–5 mm thickness (Figs. 3c–d). Ductile shear zones and fold hinges were mineralised only to a minor extent (Fig. 3e), as were late Alpine brittle shear zones, which overprinted existing open-space fissures with free-grown quartz crystals (Fig. 3f). Sulphides also occur disseminated in the sugar-grained quartzite, where carbonates were replaced. The age of fissure minerals, as indicated by K–Ar dating of adularia from the Albrunpass and hyalophane from the Lengenbach, is about 11 Ma (Purdy and Stalder, 1973).

Mineralogy

The Pb occurrence consists of coarse-grained, undeformed galena with minor amounts of other Cu-, As-, Sb-, and Pb-bearing sulphides and sulphosalts. The depositional succession of hydrothermal minerals can be divided into three stages: pre-ore stage, ore stage and post-ore stage (Fig. 4). A classical Alpine fissure mineral assemblage represents the pre-ore stage. It comprises quartz, adularia, muscovite, pyrite, rutile, tourmaline and dolomite. The ore stage consists of quartz, galena with small amounts of pyrite, tennantite-tetrahedrite, chalcopyrite and traces of arsenopyrite, bournonite, meneghinite, pyrrhotite and an unknown Ni–Fe–As sulphide (see below). Notable is the scarcity of sphalerite – only few grains were found. Ore partly affected by weathering ("supergene overprint" in Fig. 4) contains vugs that are partially filled with secondary minerals, mainly anglesite and cerussite, with minor wulfenite, native sulphur, galena, malachite, azurite, gypsum and greenockite.

Notable is the occurrence of REE-bearing minerals like monazite, bastnaesite, synchisite and parisite, which are spatially and temporally closely related to the sulphide occurrence. Such REE-minerals, which are typical for the Alpine fissure mineral assemblages in the paragneisses of the Monte Leone nappe (Schwanz et al., 1994), have not been reported from any other occurrence in the region hosted by Triassic rocks.

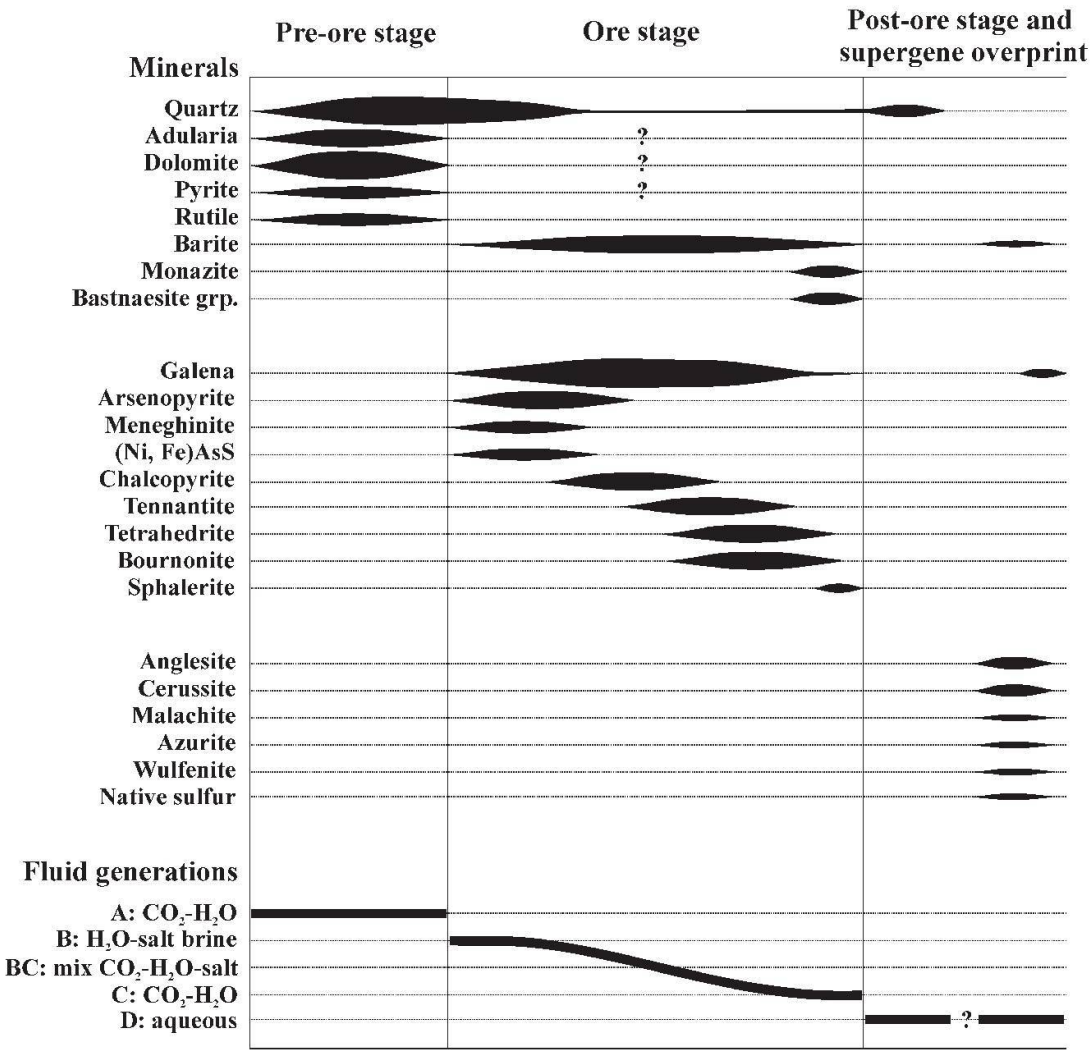

Fig. 4 Depositional succession of hydrothermal minerals at the mine site at Albrunpass as a function of the different evolutionary stages, together with the associated fluid inclusion types. Areas represent estimates of the mass proportions of the hydrothermal minerals.

Sulphide chemistry

EPMA analyses of galena samples from the study area show relatively low contents of minor and trace elements: Ag, Sb, Te, Cd, Cu and Se (see Appendix Table 1). The galena has relatively low contents of Ag (300–1500 μg/g) and Sb (400–1900 μg/g). Graeser (1969) reports concentrations in galena of 2550 μg/g Ag and 1550 μg/g Sb from the same locality. The whole spectrum of the tennantite–tetrahedrite solid solution is present in the studied area, each locality having a different, narrow range of compositions (Fig. 5). These minerals commonly show an Sb-enriched rim. The fahlores have Fe and Zn contents of 4300 to 54'000 μg/g and 24'700 to 72'100 μg/g, respectively, highly variable Ag (1400–24'200 μg/g), and traces of Sn (200–2400 μg/g), Se (200–1000 μg/g) and Cd, respectively (Appendix Table 1).

An accessory, anisotropic sulphide mineral resembling arsenopyrite was identified in polished sections. EPMA analyses of the idiomorphic grains suggest the presence of an unknown Ni–Fe–As–S phase with the following chemical composition: 19.7 wt% Ni, 15.3 wt% Fe, 44.5 wt% As, 20.7 wt% S, 0.3 wt% Cu and 0.2 wt% Se; S=100.70 wt%. This translates into the chemical formula: $(Ni_{0.56}, Fe_{0.45})_{S=1.01}As_{0.99}S_{1.07}$. XRD data reveal a possible relationship to gersdorffite-$Pca2_1$. Best results were obtained by refining the X-ray data according to the procedure of Holland and Redfern (1995), assuming the mineral to be orthorhombic: a = 5.61(2) Å, b = 5.64(7) Å, c = 5.61(1) Å (gersdorffite-$Pca2_1$: a=b=c 5.693 Å). The crystal size of < 100 μm and the intimate intergrowth with chalcopyrite and tennantite precluded single crystal XRD for the determination of the space group. A similar unknown mineral with a chemical formula of $(Ni_{0.37}, Fe_{0.25}, Co_{0.24})_{S=0.86}As_{1.06}S_{0.94}$ was reported from Pechenga, Kola Peninsula, Russia (Abzalov and Polezhaeva, 1989).

Fluid inclusion petrography

Detailed petrographic observations of crosscutting relationships between fluid inclusion trails and their spatial arrangement in the free-grown quartz crystals allowed five main successive generations of fluid inclusions to be distinguished:

(A) Early CO_2–H_2O inclusions (Fig. 6a)
(B) Aqueous brine inclusions with at least 3 daughter crystals (Fig. 6b)
(BC) Intermediate CO_2-bearing brine inclusions (Fig. 6c and 6e–f)
(C) Late CO_2–H_2O inclusions (Fig. 6d)
(D) Secondary two-phase aqueous inclusions (Fig. 6h)

Besides these, sulphide inclusions (up to 2 mm in size; (S); Fig. 6g) are lined along pseudosecondary trails petrographically identical to (BC)-type inclusions.

Early three-phase CO_2–H_2O inclusions (generation A) are characterised by the presence of liquid and vapour CO_2 and an aqueous fluid phase. The estimated H_2O volume fraction ranges from 20 to 40%, and the inclusions usually have two tiny opaque daughter crystals. Inclusions of this generation occur only in early pseudosecondary trails, generally near the base of the quartz crystals. These inclusions can be very large (exceeding 1000 µm) and often show isometric negative crystal shape (Fig. 6a).

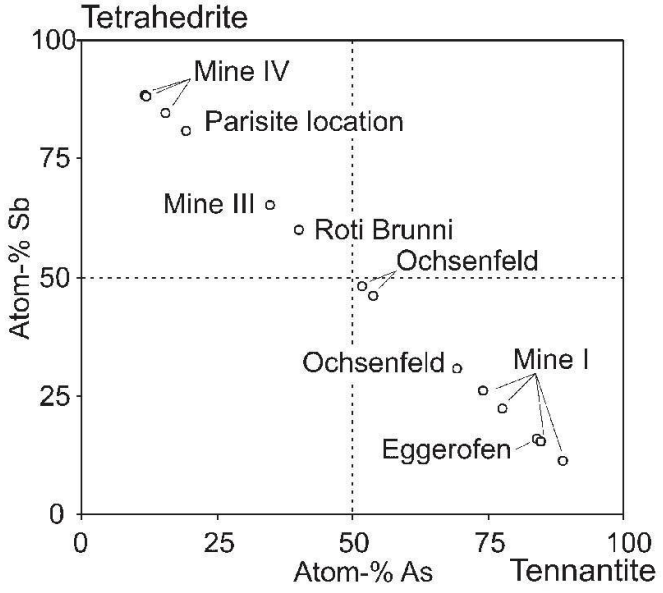

Fig. 5 Electron microprobe data for minerals of the tetrahedrite-tennantite solid solution from the studied occurrences reveal an almost complete series of tetrahedrite-tennantite solid solutions. For localities refer to Fig. 2.

The next younger generation (B) is represented by aqueous brine inclusions (Fig. 6b). These inclusions always have at least three daughter crystals of constant volume proportions: halite, calcite (as identified by Raman microspectrometry) and an unidentified Ba-bearing daughter mineral that forms colourless, transparent, birefringent crystals of orthorhombic or hexagonal habit. Larger inclusions contain opaque daughter crystals. The volume fraction of vapour is 10–20%. The inclusions are nicely negative-crystal-shaped, flat and mostly between 5 and 20 µm (occasionally up to 60 µm) in diameter. Brine inclusions only occur along pseudosecondary trails that cut younger quartz growth zones relative to the pseudosecondary trails of the early three-phase CO_2–H_2O inclusions (A).

Late three-phase CO_2–H_2O inclusions (generation C) cut trails of (A) and (B). The H_2O volume fraction of this generation varies between 10 and 30%. Daughter crystals were never observed. Inclusions of generation (C) are often flat and usually small (<15 µm), conspicuously smaller than generation (A), but show very nice negative crystal shapes and are commonly trapped on late pseudosecondary trails (Fig. 6d).

One group of fluid inclusions collectively labelled (BC) consists of aqueous liquid plus liquid and vapour CO_2 and occasional daughter crystals at variable phase proportions at room temperature (Fig. 6c and e–f). The volume fraction of H_2O is up to ~70% for the inclusions with salt daughter crystals (BC1), for the others it varies between 10 to 40%. Inclusions without daughter crystals (BC2) resemble inclusions of generation (C) very much in terms of size, shape and filling ratios. Fluid inclusions of generation (BC) occur in two distinct arrangements. They form pseudosecondary trails together with inclusions of generation (B), where the two different types of fluid inclusions form patches that are spatially separated from each other (Fig. 6e–f). Sometimes, inclusions of (B) and (BC) occur on a single trail, and it is here where the high-salinity (BC1) inclusions with daughter crystals occur.

The latest fluid inclusion generation consists of very flat, irregularly shaped aqueous inclusions on poorly healed secondary trails (Fig. 6h). The liquid to vapour ratio is 95:5. These inclusions clearly post-date those associated with the ore-forming event and are thus not considered any further.

Fluid inclusion microthermometry

Heating and freezing experiments were carried out in order to determine the molar composition

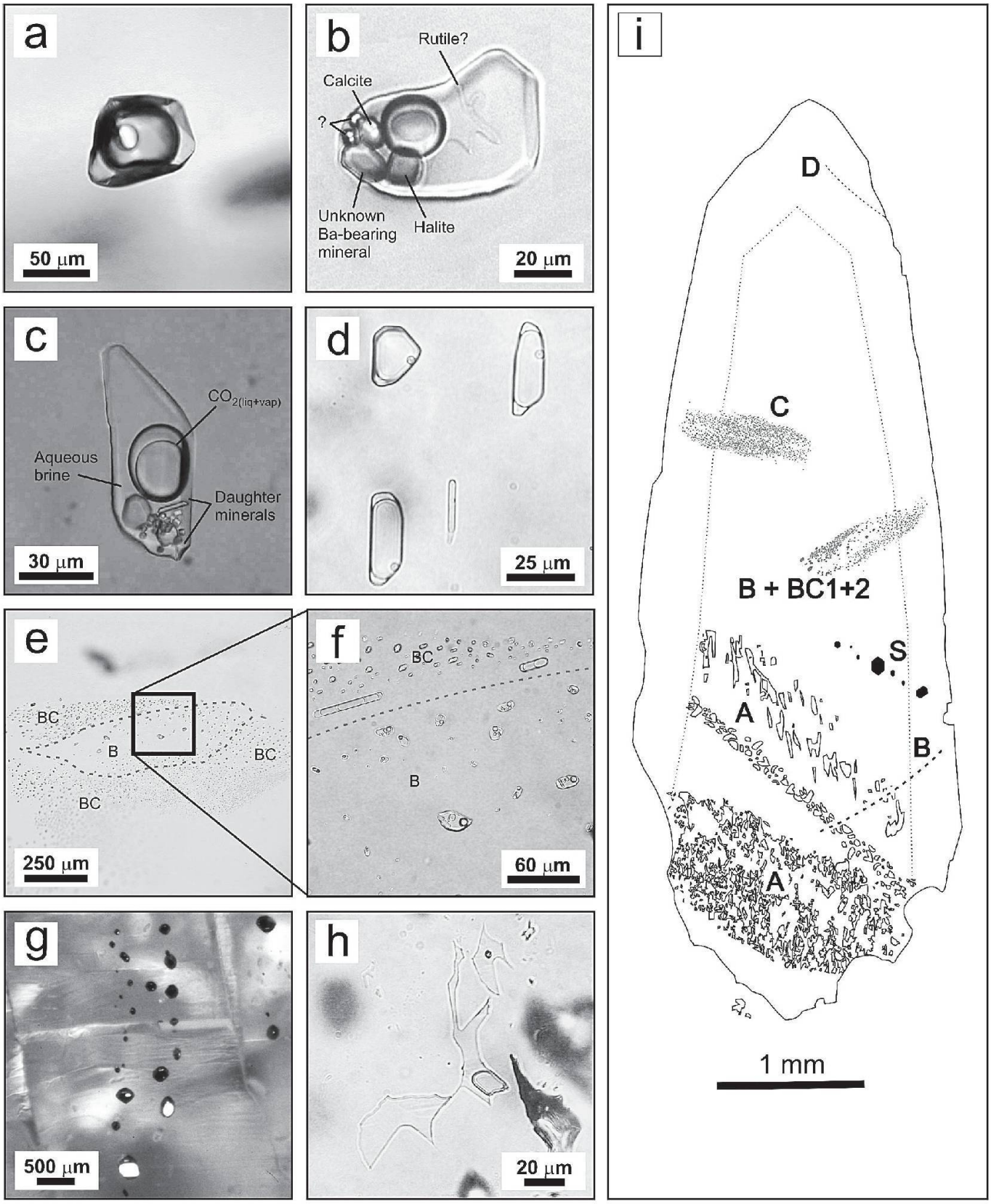

Fig. 6 Microphotographs of fluid inclusions of the different evolutionary stages in quartz from the mine site II (compare Fig. 2) (a) Three-phase CO_2-rich inclusion of generation (A) with liquid and vapour CO_2 and a low-salinity aqueous solution; (b) Aqueous brine (generation B) with multiple daughter crystals; (c) Intermediate brine with liquid and vapour CO_2 (generation BC1); (d) CO_2-rich inclusions of generation (C) with liquid and vapour CO_2 and a low-salinity aqueous solution; (e) Coexistence of fluid inclusions of generation (B) and (BC) on one pseudosecondary trail, revealing heterogeneous entrapment, and a detail shown in image (f); (g) Galena inclusions on a pseudosecondary trail in combined transmitted and reflected light (hence the bright reflection of negative crystal faces of the inclusions); (h) Late irregular aqueous low-salinity fluid inclusion of type (D); (i) Schematic section of a quartz crystal with the typical relative positions of the different inclusion generations.

Table 2 LA-ICPMS concentration data of fluid inclusion assemblages (averages of single inclusion analyses).

assemblage	sample	$NaCl_{equiv.}$ [wt%]	N	**Na** [µg/g]	1 stdev [abs]	**Mg** [µg/g]	1 stdev [abs]	**K** [µg/g]	1 stdev [abs]	**Ca** [µg/g]	1 stdev [abs]	**Mn** [µg/g]	1 stdev [abs]	**Fe** [µg/g]	1 stdev [abs]	**Cu** [µg/g]	1 stdev [abs]	**Zn** [µg/g]	1 stdev [abs]
A	LK 63-11	0.5	14	1665	*142*	n.a.		142	*44*	304	*54*	11	*12*	413	*221*	n.a.		18	*11*
A	LK 63-8b	1.0	10	2875	*170*	n.a.		494	*215*	3197	*1211*	32	*24*	425		n.a.		35	
A	LK 63-8b	2.0	2	7169	*138*	n.a.		1113	*1053*	< 13159		< 82		807		n.a.		62	
B	LK 63-13-4	31.3	6	70498	*16278*	190		14754	*7965*	48990	*35299*	951	*228*	2377	*1101*	< 267		6064	*1337*
B	LK 63-13-5	31.3	4	59880	*10756*	192		11127	*3002*	50451	*35876*	717	*253*	4433	*1727*	< 239		7740	*2589*
B	LK 63-12b	31.3	10	73517	*12237*	239	*108*	15504	*7622*	24706	*5972*	1007	*389*	3308	*842*	172	*211*	5620	*2126*
BC1	LK 63-13-5	25	1	47814		n.a.		9176		48141		971		3305		n.a.		6104	
BC2	LK 63-13-5	7.3	1	6509		n.a.		< 3247		< 49916		< 318		< 12209		n.a.		< 837	
BC2	LK 63-13-4	6.5	1	13234		n.a.		12192		< 160204		< 911		< 5785		n.a.		3504	
BC2	LK 63-13-5	5.0	2	9695	*6031*	n.a.		1111		24609		104		2208		n.a.		< 192	
C	LK 63-13-3	1.9	3	3053	*1326*	n.a.		1248	*463*	8884	*1976*	438		434		n.a.		< 56	
C	LK 63-8a	1.9	5	5597	*1409*	n.a.		721		< 7600		164		1159	*271*	n.a.		169	*126*
C	LK 63-8a	1.8	4	6735	*207*	n.a.		709	*495*	913		7		< 828		n.a.		< 84	
C	LK 63-13-1	1.2	3	4326	*402*	n.a.		395		< 6577		< 37		762	*230*	n.a.		< 67	
C	LK 63-13-2	1.1	5	3471	*537*	n.a.		1056	*143*	< 9202		135		704	*581*	n.a.		93	

assemblage	sample	$NaCl_{equiv.}$ [wt%]	N	**As** [µg/g]	1 stdev [abs]	**Rb** [µg/g]	1 stdev [abs]	**Sr** [µg/g]	1 stdev [abs]	**Ag** [µg/g]	1 stdev [abs]	**Sb** [µg/g]	1 stdev [abs]	**Cs** [µg/g]	1 stdev [abs]	**Ba** [µg/g]	1 stdev [abs]	**Pb** [µg/g]	1 stdev [abs]
A	LK 63-11	0.5	14	79	*31*	2.6	2.5	2.8	*1.3*	5.1	*3.3*	5.0	*4.6*	5.7	*10.2*	40	*15*	23	*9*
A	LK 63-8b	1.0	10	689	*290*	2.1	*1.1*	2.1	*1.2*	6.5		17	*6.5*	0.5		44	*52*	< 3.4	
A	LK 63-8b	2.0	2	304	*55*	< 9.0		9.8		< 19		20		< 3.4		73		< 13	
B	LK 63-13-4	31.3	7	467	*65*	60	*12*	4125	*969*	12		149	*50*	84	*68*	74978	*27698*	12700	*1605*
B	LK 63-13-5	31.3	4	558	*269*	45	*5.3*	4237	*878*	< 70		159	*63*	66	*31*	97758	*12465*	13659	*2977*
B	LK 63-12b	31.3	10	505	*201*	57	*32*	4866	*1852*	45		148	*73*	106	*94*	99233	*36425*	12395	*2813*
BC1	LK 63-13-5	25	1	843		63		4312		< 34		180		69		81935		11304	
BC2	LK 63-13-5	7.3	1	< 511		136		126		< 110		< 111		< 26		1998		242	
BC2	LK 63-13-4	6.5	1	< 1593		< 191		1231		< 368		796		< 69		17517		4181	
BC2	LK 63-13-5	5.0	2	332		14		194	*183*	< 21		85	*32*	8.4	*4.2*	2777	*1805*	556	*497*
C	LK 63-13-3	1.9	3	162	*43*	< 6.8		4.2	*0.6*	11	*5.2*	105		8.2		140	*51*	14	
C	LK 63-8a	1.9	5	208	*99*	< 7.8		25	*14*	25	*5.7*	569		75	*140*	941	*682*	108	*36*
C	LK 63-8a	1.8	4	689	*293*	< 9.0		2.7	*2.5*	1.5		209	*283*	40	*48*	58		< 10	
C	LK 63-13-1	1.2	4	125	*87*	< 5.9		3.0		< 11		17	*5.3*	15	*11*	77		27	*2*
C	LK 63-13-2	1.1	4	89	*65*	22		2.8		< 20		31	*7.3*	7.3		< 19.3		35	*20*

<value—concentrations below the limit of detection (see text)
n.a.—not analysed

(major components $NaCl_{equiv}$, H_2O, CO_2) of the fluid inclusion assemblages trapped during successive stages of vein formation, and to derive estimates on temperature of the ore-forming event. These data are reported in Table 1.

The average melting temperatures of CO_2 in (A), (BC) and (C) are uniformly at about –56.6 °C, which implies the absence of significant amounts of other gas species. The CO_2 homogenisation temperatures evolve along the entrapment sequence, from 11–26 °C for (A) to 29–30 °C for (BC) and 26–30.5 °C for (C). The CO_2 in most of the fluid inclusions of generations (A), (BC) and (C) homogenises through the dew point transition, while only a few show critical behaviour. Total homogenisation temperatures of fluid inclusions of generation (A) and (B) are ~240 °C and of generation (C) around 270 °C on average, respectively. Only small inclusions could be measured for their total homogenisation temperature, because large inclusions decrepitated before. Homogenisation temperatures of trails containing heterogeneously trapped inclusions of generation (BC) are around 270 °C.

The bulk salinity of fluid inclusions evolves conspicuously across the entrapment sequence. The early CO_2-rich fluid of generation (A) is characterised by low salinities of 0.5 to 2 wt% $NaCl_{equiv}$. Brines of generation (B) show a narrow range in salinity of 30.2 to 31.9 wt% $NaCl_{equiv}$. The late CO_2-rich fluid (C) has salinities between 1.1 and 1.9 wt% $NaCl_{equiv}$, and the aqueous fluid (D) contains only 1.4 wt% $NaCl_{equiv}$. Heterogeneously trapped inclusions of generation (BC) show a range in salinity between 5 and 28 wt% $NaCl_{equiv}$.

Molar proportions of the major fluid components were calculated from microthermometry and LA-ICPMS data (using the formulae after Mullis et al., 1994). As shown in Fig. 7 the molar H_2O–CO_2-salt ratio for generation (A) is: 44 : 55 : 1; for generation (B): 87 : 0 : 13; for high-salinity inclusions of generation (BC1): 79 : 10 : 11 and for lower-salinity inclusions of generation (BC2): 46 : 47: 7; and for generation (C): 29 : 70 : 1. Table 1 provides more detailed information about the molar proportions of species in the fluid inclusions with concentrations of major fluid components (Na, K, Ca, Ba, Zn and Pb) determined by LA-ICPMS.

Raman spectrometric data

The daughter crystals of inclusions of generation (B) were tested by Raman, but only one daughter mineral could be identified positively as calcite, based on the lines 1087.8, 712.2 and 281.1 cm^{-1} (Burke, 2001). A colourless daughter mineral of orthorhombic to hexagonal shape, firstly believed to be barite, remains unidentified. The most prominent Raman lines are at 3455, 3327 and 3284

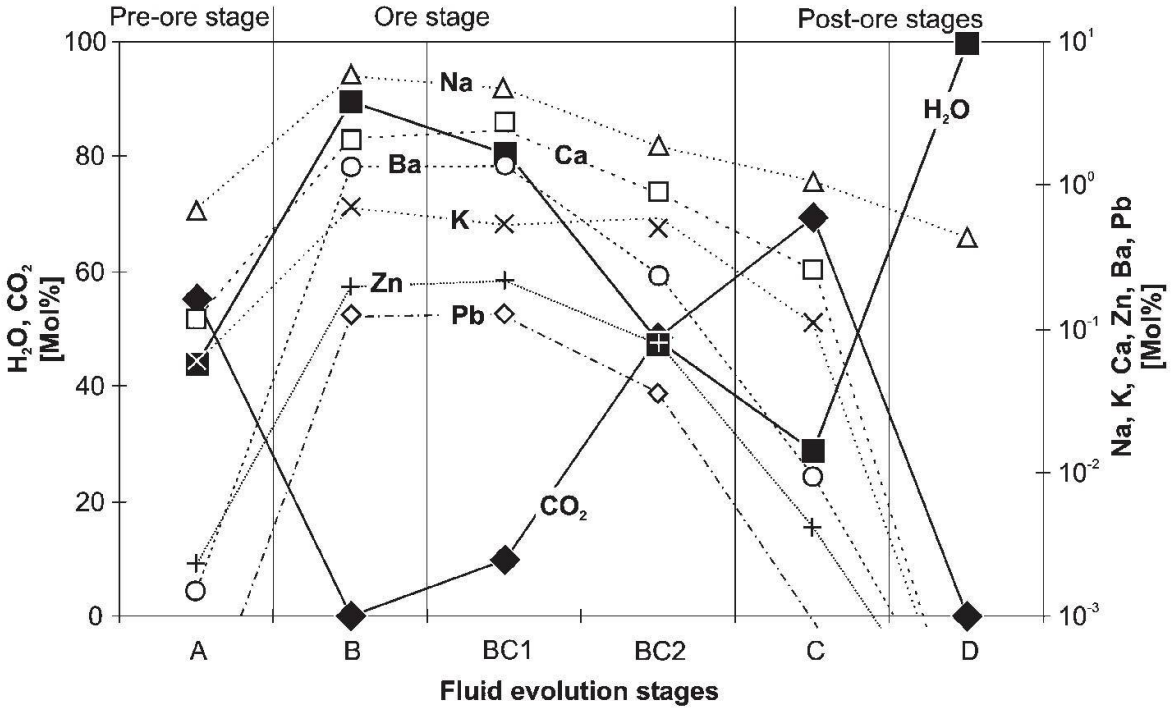

Fig. 7 Average molar concentrations of H_2O and CO_2 (left, derived from microthermometry) and of Na, K, Ca, Zn, Ba and Pb (right, from LA-ICPMS) in the fluid plotted as a function of progressive fluid stages defined by petrography. Refer to Fig. 6 for the different fluid stages. Note the conspicuous increase of element concentrations with incursion of brine stage (B).

Table 3 LA-ICPMS composition data of individual sulphide inclusions in quartz.

LA-ICPMS shot #	mineral	Pb [µg/g]	S [µg/g]	Fe [µg/g]	Cu [µg/g]	Zn [µg/g]	As [µg/g]	Ag [µg/g]	Sb [µg/g]	Bi [µg/g]
jr24b04	gn	864976	132715	22.8	119	11.7	4.6	792	1280	79
jr24b05	gn	864851	132643	8.5	180	3.5	3.9	877	1353	80
jr24b06	gn	864899	132629	8.3	152	7.9	3.3	850	1367	82
jr24b07	gn	864854	132702	49.3	217	2.7	4.0	797	1294	80
jr24b08	gn	864875	132572	5.3	200	2.8	3.3	837	1425	81

gn—galena

cm^{-1}. Recall that salt daughter crystals are not Raman active.

In the vapour bubble of generation (B) inclusions, CO_2 could be detected (lines 1388.8 and 1285.5 cm^{-1}; Burke, 2001). H_2S was detectable in the liquid CO_2-phase of inclusions of generation (A) but not in (B) and (C), based on the line 2612.4 cm^{-1} (Salmoun et al., 1994). Other gas species, like CH_4 and N_2 were not detected, consistent with microthermometric results.

LA-ICPMS concentration data of fluid inclusions

The solute concentrations of the early and late CO_2-bearing inclusions, the aqueous brine and partial mixtures thereof are presented in Table 2 as mean values of assemblages measured. Data for 71 individual inclusions are reported in the Appendix Table 2. Brine inclusions were analysed for 17 elements, and the low-salinity, CO_2-rich inclusions for 15 elements, respectively.

Figure 8 shows the metal concentrations of the different fluid assemblages across the fluid entrapment history. Sodium is always the most abundant element. The total cation concentration in the fluid of generations (A) and (C) is very low, ranging from 100 to 500 µmol/g. The total cation concentration of the brine (B) is between 3000 and 5000 µmol/g. All measured elements show higher concentrations in the brine relative to those of the pre-existing CO_2-bearing fluid. The brine contains remarkably high concentrations of Ba (on average 9 wt%, 660 µmol/g) and Pb (1.3 wt%, 63 µmol/g; Fig. 9). The metal concentrations of fluid assemblages (B) and (BC1) are identical within uncertainty (Table 2), and decline with progressive entrapment of (BC1) over (BC2) to (C), down to levels indistinguishable from generation (A).

Element ratios monitor the relative enrichment of Pb, Zn and Ba with respect to the alkali elements in the brine and the effect of precipitation and dilution on the ore metals during fluid evolution (Fig. 9). Molar Pb/Ba ratios remain constant during fluid evolution from (B) to (C), whereas molar Zn/Ba ratios slightly increase from ~0.15 to 0.4. The molar Pb/Na, Zn/Na and Ba/Na ratios evolve over one to two orders of magnitude across the evolutionary sequence and the molar Zn/Pb ratios increase from about 1.5 to 6.

Sulphide inclusions (generation (S); Fig. 6g) were analysed (Table 3) and identified as galena with Ag (800 µg/g) and Sb (1300 µg/g) concentrations similar to the bulk ore (Appendix Table 1). These inclusions have the morphology of negative quartz crystals and are aligned along pseudosecondary trails in quartz crystals. They are petrographically related to fluid inclusions of generation (BC).

Discussion

The data are now discussed in two sections. A short assessment of the reliability of the LA-ICPMS fluid inclusion data precedes the discussion of the genetic constraints on the lead occurrence at Albrunpass in the Binn Valley.

Reliability of the LA-ICPMS fluid inclusion data

Our results demonstrate that CO_2-rich fluid inclusions of variable salinity (down to 0.5 wt% $NaCl_{equiv}$) can be analysed reliably by LA-ICPMS. The ablation process is steady and controllable even for very large inclusions (up to 80 µm). The conspicuous signal spike in the beginning of an inclusion signal (Fig. 10) is observed for all ablations of CO_2-rich inclusions and is interpreted to represent release of overpressure upon opening, and the hump-shaped bulk part of the transient signal corresponds to ablation of the aqueous phase containing the dissolved salts and wetting the inclusion walls. The transient signals also provide qualitative information about the composition of daughter crystals. This aids in identifying the daughter crystals in brine inclusions and, consequently, provides constraints on the presence of aqueous species other than chlorides. This knowledge is essential to performing the appropriate salt correction during quantification, which has a

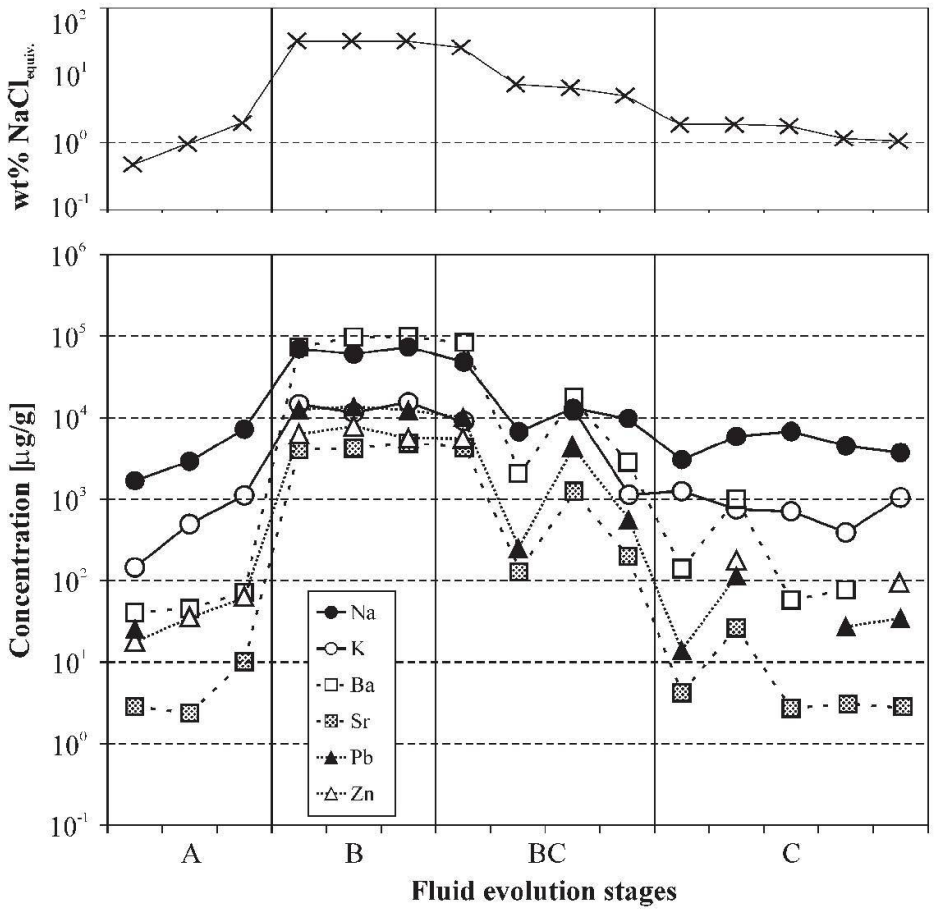

Fig. 8 Element concentrations (determined by LA-ICPMS) of individual fluid inclusion assemblages across the evolutionary fluid stages. Note the conspicuous increase of element concentrations with incursion of the brine stage (B). For molar abundances of major cations refer to Fig. 7. For standard deviations on the single fluid inclusion assemblages please refer to Table 2.

profound effect on the absolute element concentrations of fluid inclusions (Heinrich et al., 2003). For example, the LA-ICPMS signals demonstrate that Ba is a major component of one of the large daughter crystals, yet Raman spectroscopy revealed that it is not barite. Two scenarios can now be envisaged for data reduction, (1) assuming that all Ba is present as a chloride and (2) that no significant Ba is present as a chloride. Scenario (1) requires $BaCl_2$ to be included in the salt correction, while scenario (2) does not. These two scenarios were quantified for the current dataset. The resulting differences in element concentrations are up to 35% in the worst case. Generally speaking, for cases where Na is the dominant cation in an aqueous fluid, and representative sampling of the inclusion contents provided during laser-ablation (Pettke et al., 2000a), the element concentration data are estimated to be accurate to within ±20% for a fluid inclusion assemblage sensu stricto. The accuracy for the present dataset is limited by the accuracy of the salt correction employed (Heinrich et al., 2003). It should be noted that element ratios in the fluid are uniquely defined by the use of external standardisation only (i.e., uncertainties are purely analytical) and are thus insensitive to the type of salt correction employed. Therefore, the accuracy on element ratios is of the order of ±10% or better, because it chiefly depends on the analytical reproducibility of single inclusions that belong to an assemblage.

The genesis of the lead occurrence at Albrunpass

The numerous small base metal sulphide occurrences in the Binn Valley commonly contain exotic and complex sulphides and sulphosalts (Graeser, 1965). The primary sulphide mineralisation at Albrunpass is strongly dominated by galena, but the occurrence of other sulphides and sulphosalts as minor components makes it typical for the area. These minerals overgrow a classical Alpine-type fissure mineral assemblage, and they also form cm-sized replacement veins and disseminations, by dissolving carbonate in the host quartzite. Open space fissures formed periodically during retrograde stages of the Alpine orogeny. Ongoing shear deformation of the Triassic rocks

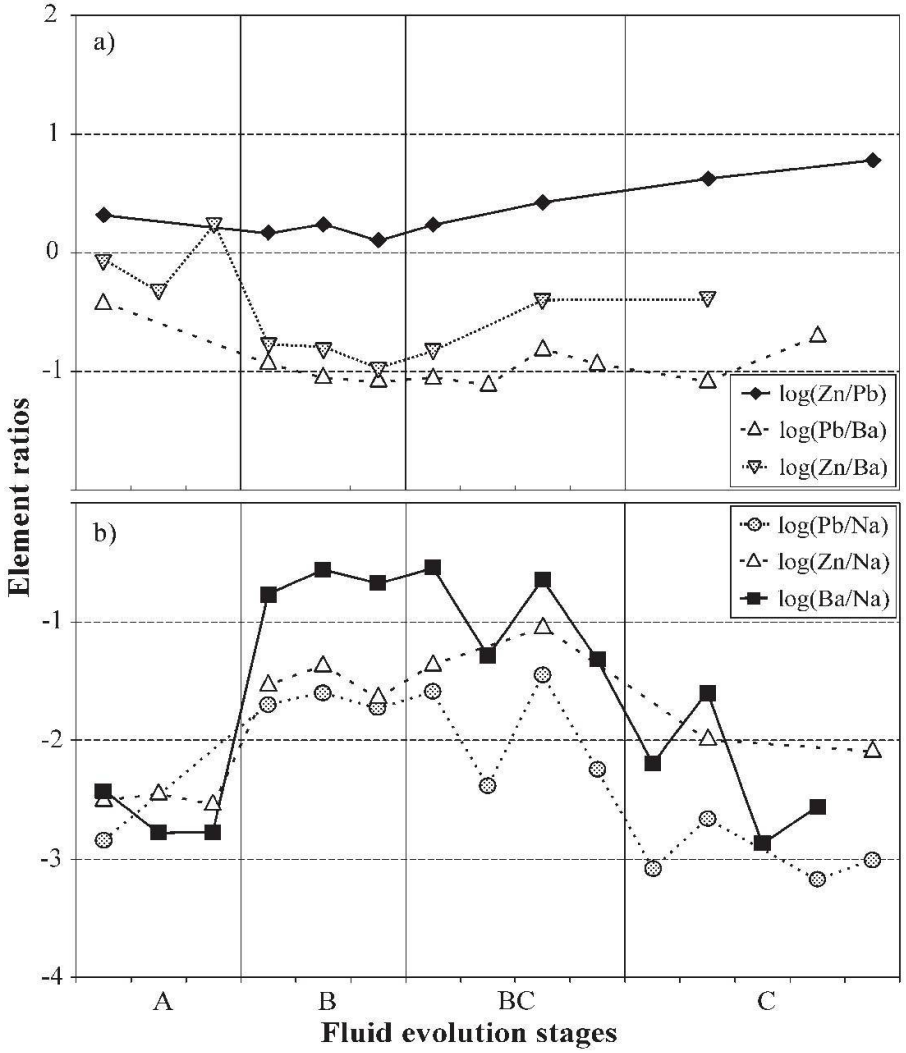

Fig. 9 Trends in element concentration ratios with fluid evolution. Data points represent averages of individual inclusion assemblages. Note the steady increase of molar Zn/Pb and Zn/Ba ratios, respectively decrease of molar Pb/Na and Ba/Na ratios, from the input fluid (B) to the spent fluid (C) in the ore stage, while the molar Pb/Ba ratio remains uniform. These trends are consistent with precipitation of galena and barite but no sphalerite.

closed some of the early open-space fissures as evidenced by quartz nodules with relics of free-grown quartz crystal faces.

Relatively little barite was found in the field, although increasing Zn/Ba ratios in the evolving fluid suggest that significant amounts of barite formed during mineralisation. This might be due to the fact that the occurrence was mainly mined out in the 16th century. The historic reports of high grade Ag ore (4% in galena; Archivio di Stato di Milano, 1576) cannot be confirmed here, assuming that Ag concentrations are uniform across the occurrence. Our EPMA data show that the concentration of Ag in galena (dominating the mass of the ore) does not exceed 1500 μg/g, and the LA-ICPMS data of the fluid inclusions suggest that the ore-forming fluid contained below ~50 μg/g Ag. Unless the occurrence did not contain a much greater proportion of fahlores (containing up to 1.3 wt% Ag; Appendix Table 1) than implied by present-day findings, it can be concluded that the occurrence probably did not produce much Ag.

Phase proportions and microthermometric properties of fluid inclusion generations (A), (B), (C) and (D) all indicate homogeneous entrapment. In contrast, coexistence of brine inclusions (generation B) with CO_2-bearing inclusions of variable salinity (BC) on single trails (Fig. 6e–f) points to heterogeneous entrapment. The entrapment sequence of fluid inclusion types with CO_2-bearing low-salinity fluids at pre- and post-ore stages, and the close temporal relationship between high-salinity brines and aqueous fluids of variable salinity and CO_2 contents provides evidence for the coexistence of partly miscible fluids (Diamond, 2001) followed by progressive dilution of the metal-charged brine by the CO_2-bearing

fluid during stage (BC). Temperatures of total homogenisation of fluid inclusions from assemblages of co-existing aqueous brine and high-CO_2 fluids during stage (BC) confine the temperature of ore precipitation of the ore stage to about 270 °C. The measured increase in CO_2 homogenisation temperatures across the fluid entrapment sequence reflects an increase in the bulk molar volume of the fluid, hence corresponds to a decrease in its bulk density. This may indicate a decrease in fluid pressure during ore precipitation in response to the late Alpine decompression of the Central Alps. Collectively, this evidence points to an emplacement of the sulphide occurrence at a very late stage during the retrograde Alpine metamorphic history.

The galena inclusions (S) located on pseudosecondary trails are additional evidence for the hydrothermal formation of the occurrence. Hofmann (1994) suggested the presence of a sulphide melt during the formation of the Lengenbach deposit. However, the melting temperature of pure PbS is 1114 °C. Peak metamorphic temperature reached in the region is estimated to 550 °C (Todd and Engi, 1997) and the temperature of ore formation at Albrunpass is estimated to <300 °C. Therefore we could not find any evidence for the presence of a sulphide melt during ore formation at Albrunpass.

Fluid chemistry and precipitation mechanisms

In agreement with the deduction from the major chemical species (CO_2–H_2O-salt) of the various inclusion generations, the concentrations of the major cations in the fluid inclusions also document the incursion of the brine (B) into the pre-existing CO_2-rich, aqueous low-salinity fluid (A). The concentrations of the cations increase by up to three orders of magnitude from fluid (A) to (B) (Fig. 8). The progressive salinity decrease in fluid assemblages of stage (BC) suggests that a single

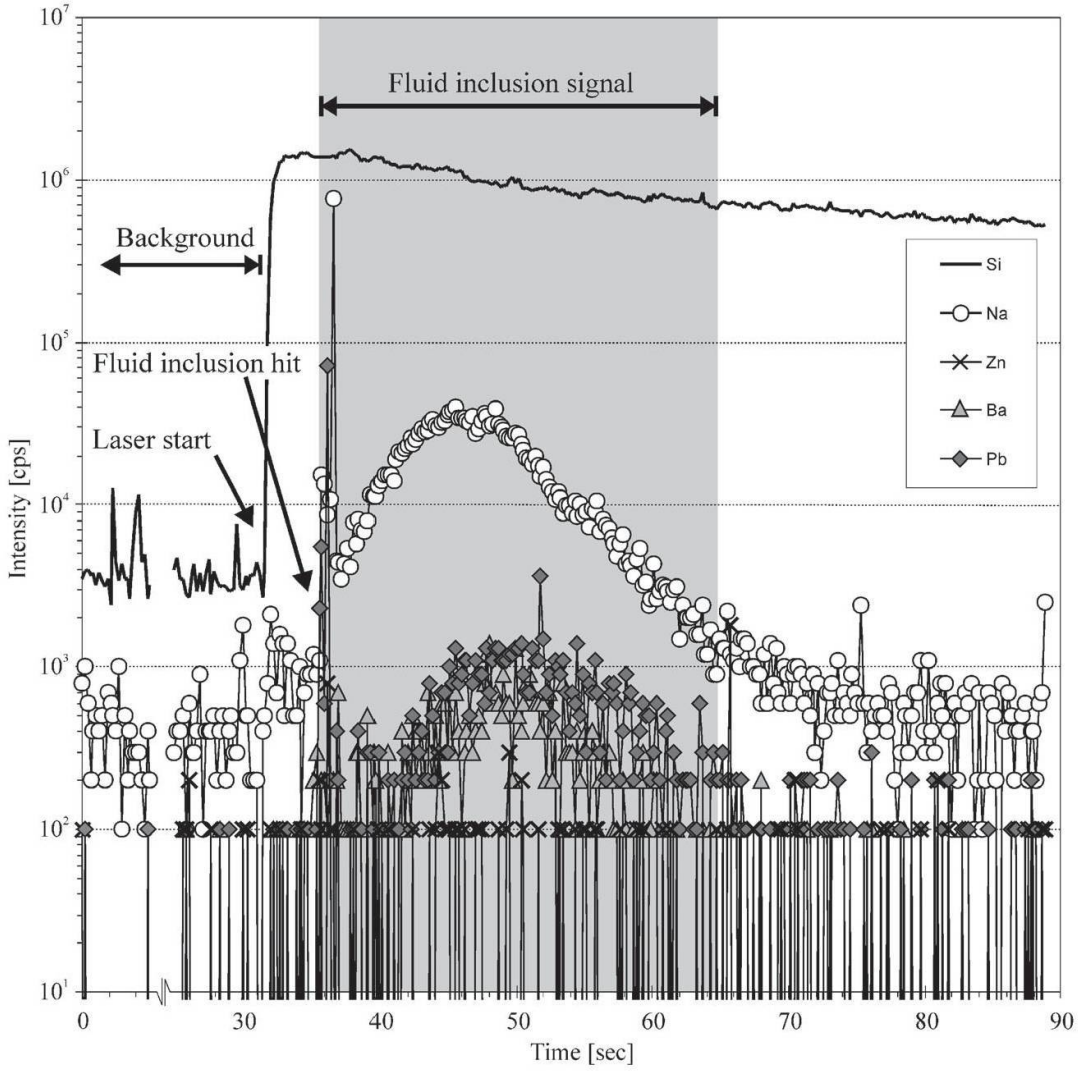

Fig. 10 Transient LA-ICPMS signal of a CO_2-rich inclusion with the typical spike at the time the inclusion is opened by the laser, corresponding to a sudden internal pressure release, followed by a smooth curve while the inclusion is ablated entirely.

pulse of metal-charged brine infiltrated a large mass of low-salinity, metal-poor aqueous CO_2-bearing fluid. These two fluid types did not mix instantaneously, as evidenced by heterogeneously trapped brine and CO_2-bearing inclusions within the same trail. Rather, progressive dilution of the brine (B) by the aqueous CO_2-bearing fluid (A) occurred until all the brine was consumed. This process is illustrated both by the decreasing bulk salinities ($NaCl_{equiv}$, as determined by microthermometry, Fig. 8a) and by the decreasing element concentrations (as determined by LA-ICPMS), with generation (C) approaching the values in the pre-existing fluid generation (A) (Fig. 8).

Across this evolutionary sequence, the measured element ratios resolve the effects of pure dilution and of specific mineral precipitation. The molar Zn/Pb ratios, for example, evolve from about 1.5 in generation (B) to 6 in (C) (Fig. 9), reflecting the favoured precipitation of PbS relative to ZnS. In fact, sphalerite occurs only accessorily in the ore. The molar Zn/Ba ratios concurrently evolve from ~0.15 to 0.4, recording Ba deposition as barite, while keeping the bulk Zn in solution. Contemporaneous precipitation of galena and barite from the solution is consistent with the measured Pb/Ba-ratios, which remain relatively uniform across this evolutionary sequence. The highly selective character of precipitation of galena relative to sphalerite relates to the initial abundances of Pb and Zn and to the much higher solubility of ZnS in saline aqueous fluids under virtually any conditions (reduced-sulphur activity $a_{S(r)}$, and pH), at any given temperature between 25–300 °C (Barrett and Anderson, 1988).

Because Zn remained essentially in solution during galena precipitation, the mass ratios of the brine (B) and the pre-existing, aqueous CO_2-bearing fluid (A) can be estimated. It is assumed that the concentration of Zn in the fluid inclusions of the pre-ore generation (A) fluid (24 μg/g on average) is initial and undisturbed. Compared with the concentration of Zn in the post-ore generation (C) fluid (144 μg/g on average) – this represents the amount of Zn in the spent ore fluid – the contribution of Zn from the admixed ore-forming brine (B) to the fluid (A) is $[Zn]^C - [Zn]^A = 144–24 = 120$ μg/g. The ratio of the Zn concentration in the brine (on average 6177 μg/g) and the concentration of added Zn in (C) after complete dilution (120 μg/g) is equivalent to the mass ratios of the brine to the CO_2-rich fluid (generation A) involved in the mixing process. This ratio (B):(A) is approximately 1:50. These mass-balance considerations and the small size of the occurrence suggest that only a limited amount of metal-rich brine was involved in the formation of the occurrence.

Raman analyses revealed the presence of H_2S in the pre-ore generation fluid (A), but H_2S could not be detected in the ore-stage fluid (B) and the post-ore fluid (C). Therefore, the incursion of the brine into an H_2S-enriched environment and the concurrent increase of the H_2S activity relative to the concentration of dissolved metals (Fig. 11) in the mixture may constitute an important precipitation mechanism. Microthermometry indicates, however, that H_2S is not a major component of the generation (A) fluid. The limited availability of reduced sulphur ($S_{(r)}$) is also presumably the reason that Zn remained in solution (Fig. 11).

Taking into account the fluid mass proportions of dilute aqueous CO_2-bearing fluid and brine (A:B = 50:1) and assuming that all the reduced sulphur ($S_{(r)}$) supplied by the fluid (A) was consumed during the precipitation of galena, the molar amount of $S_{(r)}$ can be estimated. The concentration of non-precipitated Pb in the spent ore fluid (C) is $[Pb]^C - [Pb]^A = 64$ μg/g–23 μg/g = 41 μg/g; relative to the brine (B), which is 50 times lower in mass: 41 μg/g × 50 = 2050 μg/g. This corresponds to the amount of Pb contained in the brine (B), that did not precipitate and, accordingly, 11'000 μg/g (= 0.053m; log m $Pb^B = -1.28$) of Pb precipitated, given the concentration of ~13'000 μg/g Pb in the brine. The same concentration of $S_{(r)}$ would be necessary to precipitate the Pb directly from the brine (B) without taking the $S_{(r)}$ from fluid (A). This amount of $S_{(r)}$ relative to the fluid mass of (A) is then: $0.053m / 50 = 1.1 \times 10^{-3}$m $S_{(r)}^A$; log m $S_{(r)}^A = -2.98$). This is the best estimate for the concentration of reduced sulphur.

Combining the measured Pb concentrations in the different fluid generations and the solubility model of Barrett and Anderson (1988), a maximum pH estimate can be derived from the estimations of the activity of reduced sulphur ($a_{S(r)}$) (Fig. 11). For generation (A), where the log m $S_{(r)}$ is constrained to about –3, the pH has to be lower than 4, otherwise PbS would have precipitated from fluid (A). The pH of the brine cannot be estimated reliably, but as indicated by carbonate-destructive wall-rock alteration, it is most probably lower than the pH of (A). The concentration of reduced sulphur in the brine (B) is deduced to be considerably lower than that of fluid (A), because Raman spectroscopy did not reveal $S_{(r)}$ in the brine. The mixture (BC) is most likely very similar to (A) in terms of pH and $a_{S(r)}$, because of the high fluid mass ratio of (A) to (B). In the fluid of generation (C) the $S_{(r)}$ is mostly spent for sulphide precipitation, the $a_{S(r)}$ is expected to be very low, and the pH is probably similar to (A) and (BC). The syn- and post-ore deposition fluids (BC) and (C) are probably not strongly undersaturated with re-

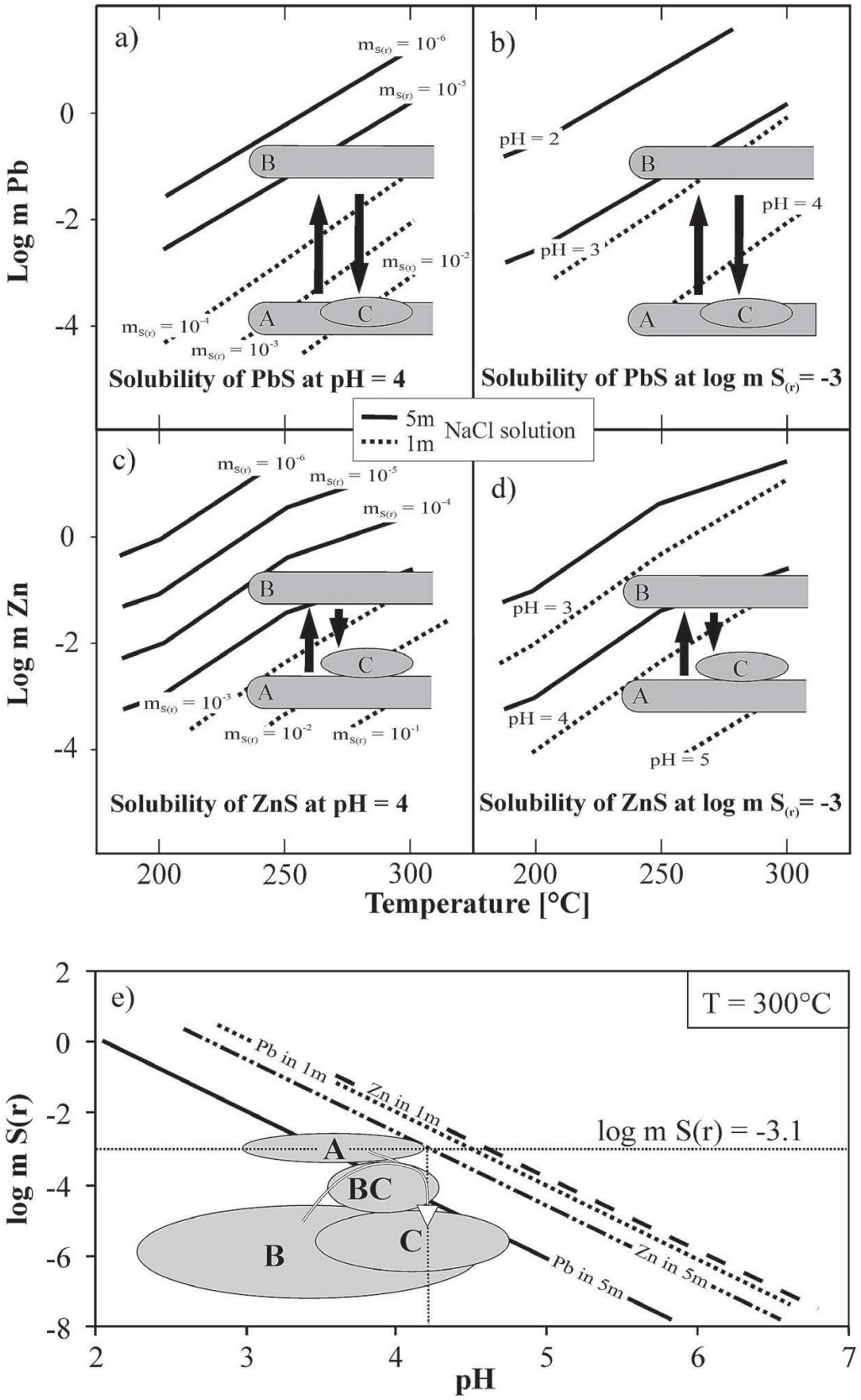

Fig. 11 Solubilities of PbS and ZnS plotted as molar concentrations (y-axis) against temperature for two bulk salinities (1m and 5m NaCl, respectively), different concentrations of reduced sulphur at constant pH (Figs. 11a and c), and variable pH at constant concentration of reduced sulphur (Figs. 11b and d). Solubility data are from Barrett and Anderson (1988). Fields A, B, BC and C correspond to the fluid stages illustrated in Fig. 6. These data illustrate that both an increase in the concentration of total reduced sulphur and an increase in pH can trigger galena and sphalerite deposition. (e) illustrates our preferred model. According to the large differences in fluid masses (A:B = 50 : 1) the incursion of a potentially acidic brine would not significantly change the pH of the ambient CO_2-rich fluid upon mixing, nor would the subordinate wall rock alteration observed. Shifts in concentration of reduced sulphur ($S_{(r)}$) upon fluid mixing are therefore identified as the main cause of sulphide precipitation.

spect to the sulphides, which constrains the range of possible pH and $a_{S(r)}$ values (Fig. 11). Given the measured Pb and Zn abundances in the brine of 13'000 μg/g (= 63 μmol/g fluid) and 6500 μg/g (= 99 μmol/g fluid), respectively, and estimated pH and $a_{S(r)}$, the mixed hydrothermal fluid becomes eventually saturated with galena but not with sphalerite, producing the observed galena-rich ore.

Fluid-rock interaction may have played only a subordinate role as a precipitation mechanism, as alteration envelopes are only few millimetres thick in the relatively porous carbonate-bearing quartzite. A hydrothermal origin of the quartzite related to the late Alpine mineralisation can be excluded, because of the dynamic recrystallisation of the quartz grains, which is not expected to occur at the temperatures estimated for the mineralisation (Voll, 1976).

Origin of fluids and metals

The Pb/Na, Zn/Na and Ba/Na ratios are very different in the early CO_2-rich fluid and the brine, demonstrating that the brine containing the ore metals and the regional-scale CO_2-dominated metamorphic fluid originate from different sources. The largest carbonate-hosted Pb–Zn deposit of the Alps, Bleiberg, is a syngenetic stratiform and vein Pb–Zn deposit of Middle to Late Triassic age (230–220 Ma; Köppel and Schroll, 1985). The metal-charged brine could thus represent a fluid from Triassic lithologies that remobilised such a type of a pre-existing metal enrichment, and the elevated contents of notably Sr and Ba (Fig. 8) suggest a genetic link with evaporites associated with Rauwacke horizons.

The CO_2-bearing fluid (generation A), on the other hand, is likely of metamorphic origin, i.e., was produced by amphibolite-facies metamorphic devolatilisation reactions at depth, possibly in Mesozoic calcareous schists (Bündnerschiefer), very much like the source of fluid for the mesothermal gold lodes of the Monte Rosa Gold District (Pettke et al., 2000b). These rocks also contain appreciable amounts of reduced sulphur, consistent with the identification of H_2S in the fluid inclusions of generation (A). The pre-Mesozoic basement gneisses of the Monte Leone nappe are unlikely to constitute a significant source for any of the fluids that were present during Alpine metamorphism. These rocks were already devolatilised during earlier high-grade metamorphic events (Biino et al., 1997), the temperature conditions of which were most likely not exceeded during Alpine metamorphism at amphibolite facies. Thus, no significant mass of fluid is expected to be released from such basement gneisses. Fluid-rock reaction of a Bündnerschiefer fluid with basement gneisses, however, is indicated by the occurrence of REE-carbonates and phosphates in close spatial and temporal relationship with the base-metal mineralisation at the Albrunpass. Sporadic and small Cu–As–REE occurrence of alpine age in the Monte Leone nappe point to a high mobility of Cu, As and REE's during Alpine metamorphism (Krzemnicki, 1992). Assuming that the CO_2-rich fluid pervasively infiltrated the rock pile, it seems unlikely that the brine travelled for a long distance before mixing with, and being diluted by, this regional-scale fluid.

Conclusions

The formation of a late Alpine base metal deposit in the Binn Valley region, Switzerland/Italy, has been investigated by detailed fieldwork and analyses of fluid inclusions by microthermometry, Raman spectrometry and LA-ICPMS. The hydrothermal system is characterised by the incursion of aqueous brine (type B) into a pre-existing, low-salinity, CO_2-dominated aqueous fluid (type A), and the progressive mixing of these two fluids. This mixture evolved towards lower and lower salinity, interpreted to monitor progressive dilution of the brine (B) by the pre-existing CO_2-dominated fluid (A). Galena but not sphalerite precipitation occurred concomitantly. The spent CO_2-rich aqueous ore fluid (type C) again closely resembles the pre-existing fluid (A). Heterogeneously trapped fluid inclusion assemblages constrain the crystallisation temperature of the ore to about 270 °C, consistent with field relations inferring ore formation during retrograde temperature stages of the Alpine tectono-metamorphic evolution.

The detailed LA-ICPMS fluid inclusion investigation demonstrates that low-salinity CO_2-rich fluid inclusions (1–2 wt% $NaCl_{equiv}$) can be analysed reliably. These data reveal a low abundance of the ore metals Pb and Zn in the early (stage A) and late (stage C) CO_2-dominated fluids. Simple modelling based on experimental data by Barrett and Anderson (1988), together with measured abundances in the brine of up to 13'700 μg/g (= 66 μmol/g) Pb and 7800 μg/g (= 119 μmol/g) Zn, the absence of significant amounts of sphalerite, and the higher solubility of ZnS relative to PbS at mineralisation temperatures of ~270 °C constrain the pH of the pre-ore CO_2-rich fluid to below ~4 and the concentration of reduced sulphur to about 10^{-3} mol/kg fluid.

Fissure formation in a brittle deformation regime at retrograde metamorphic conditions

around 11 Ma opened space for the crystallisation of a typical Alpine hydrothermal mineral assemblage. Quartz, adularia, muscovite, pyrite and rutile formed from a low-salinity S-bearing CO_2-rich aqueous fluid of most probably metamorphic origin, possibly from devolatilisation of Mesozoic calcschists, the Bündnerschiefer, at depth. Ingress of a highly metal charged brine then introduced metals to the system. The brine was most likely locally derived from Triassic evaporite units and probably had interacted with a "Bleiberg-type" Pb–Zn enrichment in order to become enriched notably in Pb and Ba. Progressive mixing of this brine with the aqueous CO_2-rich fluid resulted in an increase of metal concentrations and associated shifts in the amounts of reduced sulphur and pH of the mixed fluid relative to the brine. The increase in the activity of reduced sulphur was probably the trigger for sulphide precipitation. This genetic scenario is considered to be valid for many of the late-metamorphic galena ± sphalerite occurrences scattered throughout Triassic sediments of the Alps.

Acknowledgements

We wish to thank Susanne Schmidt for her help with EPMA and Thomas Driesner, Lluís Fontboté and Chris Heinrich for discussion at earlier stages of this work. We thank Willi Tschudin for excellent preparation of polished sections. Claudio Albertini kindly provided information about the mining history of the region. The crew of the Binntal cabin is thanked for hosting during fieldwork in 1999. Special Thanks go to Larryn Diamond and an anonymous reviewer for the constructive suggestions they provided.

References

Abzalov, M.Z. and Polezhaeva, L.I. (1989): Sulphoarsenides in rocks of productive beds of Pechenga (Kola Peninsula). *Zapiski Vses. Mineral. Obshch.* **118/4**, 64–73. (in Russian)

Angus, S., Armstrong, B., Reuk, K.M.D., Altunin V.V., Gadetskii, O.G., Chapla, G.A. and Rowlinson, J.S. (1973): International thermodynamic tables of the fluid state: carbon dioxide. International Union of Pure and Applied Chemistry. Pergamon.

Archivio di stato di Milano (1576): Pergamena del privilegio concesso il 23 aprile 1576 a Badassarre Luchsinger. Cartella Commercio 209 (ex242), fascicolo 4.

Bader, H. (1934): Beitrag zur Kenntnis der Gesteine und Minerallagerstätten des Binnentales. *Schweiz. Mineral. Petrogr. Mitt.* **14**, 319–443.

Barrett, T.J. and Anderson, G.M. (1988): The solubility of sphalerite and galena in 1–5-M NaCl solutions to 300°C. *Geochim. Cosmochim. Acta* **52/4**, 813–820.

Bianchi, G.W., Martinotti, G. and Oberhänsli, R. (1998): Metasedimentary cover sequences and associated metabasites in the Sabbione Lake zone, Formazza valley, Italy, Northwest Alps. *Schweiz. Mineral. Petrogr. Mitt.* **78/1**, 133–146.

Biino, G.G., Marquer, D. and Nussbaum, C. (1997): Alpine and pre-Alpine subduction events in polycyclic basements of the Swiss Alps. *Geology* **25/8**, 751–754.

Bodnar, R.J. and Vityk, M.O. (1994): Interpretation of microthermometric data for H_2O–NaCl fluid inclusions. In: Vivo B.D. and Frezzotti M.L. (eds.): Fluid inclusions in minerals: methods and applications. Virginia Tech, Blacksburg, Va., 117–130.

Burke, E.A.J. (2001): Raman microspectrometry of fluid inclusions. *Lithos* **55/1–4**, 139–158.

Diamond, L.W. (1992): Stability of CO_2 clathrate hydrate + CO_2 liquid + CO_2 vapour + aqueous KCl–NaCl solutions – experimental-determination and application to salinity estimates of fluid inclusions. *Geochim. Cosmochim. Acta* **56/1**, 273–280.

Diamond, L.W. (2001): Review of the systematics of CO_2–H_2O fluid inclusions. *Lithos* **55/1–4**, 69–99.

Driesner, T. and Heinrich, C.A. (2003): Accurate P-T-X-V-H correlations for the system NaCl-H_2O from 0 to 800°C, 0 to 500 MPa, and 0 to 1 XNaCl. In: Degi, J. and Szabo, C. (eds.): ECROFI XVII. Department of Mineralogy, Geochemistry and Petrology, University of Szeged, Budapest, 55–56.

Graeser, S. (1965): Die Mineralfundstellen im Dolomit des Binntales. *Schweiz. Mineral. Petrogr. Mitt.* **45**, 597–791.

Graeser, S. (1969): Minor elements in sphalerite and galena from Binnatal – Relations to coloration problems, isotopic composition, etc. *Contrib. Mineral. Petrol.* **24/2**, 156–163.

Graeser, S. and Roggiani, A.G. (1976): Occurrence and genesis of rare arsenate and phosphate minerals around Pizzo Chervandone, Italy – Switzerland. *Soc. It. Min. Petr. Rendiconti* **XXXII/1**, 279–288.

Günther, D., Audetat, A., Frischknecht, R. and Heinrich, C.A. (1998): Quantitative analysis of major, minor and trace elements in fluid inclusions using laser ablation inductively coupled plasma mass spectrometry. *J. Anal. At. Spectrom.* **13/4**, 263–270.

Heinrich, C.A., Andrew, A.S. and Knill, M.D. (2000): Regional metamorphism and ore formation: evidence from stable isotopes and other fluid tracers. In: Spry, P.G., Marshall, B. and Vokes, F.M. (eds.): Metamorphosed and Metamorphogenic Ore Deposits. *Reviews in Economic Geology* **11**, 97–117.

Heinrich, C.A., Pettke ,T., Halter, W.E., Aigner-Torres, M., Audétat, A., Günther, D., Hattendorf, B., Bleiner, D., Guillong, M. and Horn, I. (2003): Quantitative multi-element analysis of minerals, fluid and melt inclusions by laser-ablation inductively-coupled-plasma mass-spectrometry. *Geochim. Cosmochim. Acta* **67/18**, 3473–3497.

Hoefs, J. and Graeser, S. (1968): Schwefelisotopenuntersuchungen an Sulfiden und Sulfosalzen des Binnatales. *Contrib. Mineral. Petrol.* **17**, 165–172.

Hofmann, B.A. (1994): Formation of a sulfide melt during Alpine metamorphism of the Lengenbach polymetallic sulfide mineralisation, Binntal, Switzerland. *Min. Deposit.* **29/5**, 439–442.

Hofmann, B.A. and Knill, M.D. (1996): Geochemistry and genesis of the Lengenbach Pb–Zn–As–Tl–Ba-mineralisation, Binn valley, Switzerland. *Min. Deposit.* **31/4**, 319–339.

Holland, T.J.B. and Redfern, S.A.T. (1997): Unit cell refinement from powder diffraction data: The use of regression diagnostics. *Mineral. Mag.* **61/1**, 65–77.

Knill, M.D. (1996): The Pb–Zn–As–Tl–Ba-deposit at Lengenbach, Binn Valley, Switzerland. Petrogenesis based on combined geochemical and isotopical (U, Pb, Rb, Sr, S, O, C) investigations. *Geotechnische Serie* No. **90**, Schweizerische Geotechnische Kommission. Zürich, 74 pp.

Köppel, V. and Schroll, E. (1985): Herkunft des Pb der triassischen Pb–Zn-Vererzungen in den Ost- und Südalpen. *Arch. f. Lagerst.forsch. Geol. B.-A.* **6**, 215–222.

Krzemnicki, M. (1992): As–Bi-Mineralisation in der Monte Leone Decke im Mättital (Binntal Region). Unpubl. Diploma thesis, Universität Basel.

Leach, D.L. and Sangster, D.F. (1993): Mississippi Valley-type lead-zinc deposits. In: Kirkham, R.V., Sinclair, W.D., Throp, R.I. and Duke, J.M. (eds.): Mineral Deposit Modeling. *Geological Association of Canada Special Paper* **40**, 289–314.

Leu, W. (1986): Lithostratigraphy and tectonics of North-Pennine sediments in the region of Val-Bedretto, Val-Baceno and Visp. *Eclogae Geol. Helv.* **79/3**, 769–824.

Longerich, H.P., Jackson, S.E. and Günther, D. (1996): Laser ablation inductively coupled plasma mass spectrometric transient signal data acquisition and analyte concentration calculation. *J. Anal. At. Spectrom.* **11/9**, 899–904.

Lüthy, H.J. (1965): Geologie der gotthardmassivischen Sedimentbedeckung und der Penninischen Bündnerschiefer in Blinnental, Rappental und Binntal (Oberwallis). Unpubl. PhD thesis Universität Bern.

Mullis, J., Dubessy, J., Poty, B. and O'Neil, J. (1994): Fluid regimes during late stages of a continental collision – physical, chemical, and stable-isotope measurements of fluid inclusions in fissure quartz from a geotraverse through the Central Alps, Switzerland. *Geochim. Cosmochim. Acta* **58/10**, 2239–2267.

Stalder, H.A., de Quervain, F., Niggli, E., Graeser, S., Jenny, V. (1973): Die Mineralfunde der Schweiz. Wepf and Co., Basel, 433 pp.

Pettke, T., Heinrich, C.A., Ciocan, A.C. and Günther, D. (2000a): Quadrupole mass spectrometry and optical emission spectroscopy: detection capabilities and representative sampling of short transient signals from laser-ablation. *J. Anal. At. Spectrom.* **15/9**, 1149–1155.

Pettke, T., Diamond, L.W. and Kramers, J.D. (2000b): Mesothermal gold lodes in the north-western Alps: A review of genetic constraints from radiogenic isotopes. *Eur. J. Mineral.* **12/1**, 213–230.

Potter, R.W., Babcock, R.S. and Brown, D.L. (1977): New method for determining solubility of salts in aqueous solutions at elevated temperatures. *Journal of Research of the US Geological Survey* **5/3**, 389–395.

Purdy, J.W. and Stalder, H.A. (1973): K–Ar ages of fissure minerals from the Swiss Alps. *Schweiz. Mineral. Petrogr. Mitt.* **53/1**, 79–98.

Salmoun, F., Dubessy, J., Garrabos, Y. and Marsaultherail, F. (1994): Raman spectra of H_2S along the liquid-vapour coexistence curve. *J. Raman Spectroscopy* **25/4**, 281–287.

Schmidt, C. and Bodnar, R.J. (2000): Synthetic fluid inclusions: XVI. PVTX properties in the system H_2O–NaCl–CO_2 at elevated temperatures, pressures, and salinities. *Geochim. Cosmochim. Acta* **64/22**, 3853–3869.

Schroll, E. (1996): The Triassic carbonate-hosted Pb–Zn mineralisation in the Alps (Europe): The genetic position of Bleiberg type deposits. In: Sangster D. (ed.): Carbonate-Hosted Lead–Zinc Deposits. *Society of Economic Geologists Special Publication* **4**, 182–194.

Schwanz, J., Schüpbach, T. and Gorsatt, A. (1994): Das Binntal und seine Mineralien. Verlag Andre Gorsatt, Binn, 271 pp.

Spicher, A. (1988): Tektonische Karte der Schweiz 1:500 000. Schweiz. Geol. Kommission.

Todd, C.S. and Engi, M. (1997): Metamorphic field gradients in the Central Alps. *J. Metamorphic Geol.* **15**, 513–530.

Voll, G. (1976): Recrystallization of quartz, biotite and feldspars from Erstfeld to the Leventina nappe, Swiss Alps, and its geological significance. *Schweiz. Mineral. Petrogr. Mitt.* **56**, 641–647.

Received 23 September 2003
Accepted in revised form 30 March 2004
Editorial handling: A. von Quadt

Appendix

Table A1 Electron microprobe compositional data in wt% for hydrothermal sulfides from the study area.

Sample locality	Sample-#	Mineral	S	Fe	Cu	Zn	As	Se	Ag	Cd	Sn	Sb	Te	Pb	Total
Ochsenfeld	LK-2.1	tn	27.36	3.88	40.00	3.31	10.43	0.06	0.20	0.04	0.24	14.97	0	0	100.49
Ochsenfeld	LK-2.2	tn	26.98	3.88	39.02	3.46	10.37	0.07	0.18	0	0.17	15.06	0	0	99.19
Ochsenfeld	LK-2.3	tn	27.69	4.48	39.30	2.90	13.94	0.09	0.30	0	0.15	9.37	0	0	98.22
Eggerofen	LK-74	tn	28.75	3.18	42.82	3.91	15.77	0.08	0.14	0	0.03	5.37	0	0	100.05
Mine I	LK-180.04	tn	28.08	4.48	40.53	3.12	16.08	0.07	0.59	0	0.02	6.80	0	0	99.77
Mine I	LK-180.04	tn	28.53	4.67	39.14	2.69	16.77	0.10	0.46	0	0.04	5.26	0	0	97.66
Mine I	LK-180.05	tn	27.93	4.49	40.76	3.06	14.73	0.08	0.54	0	0.09	8.24	0	0	99.92
Mine I	LK.180.09	tn	27.57	5.40	42.50	2.47	17.88	0.06	1.11	0	0	3.45	0	0	100.44
Mine III	LK-182.08	tt	26.57	2.01	38.88	5.41	6.43	0.04	0.24	0	0.08	20.59	0	0	100.25
Mine IV	LK-183.08	tt	25.94	2.97	37.97	4.02	2.30	0.02	1.18	0	0.10	27.49	0	0	101.99
Mine IV	LK-183.08	tt	25.29	3.00	38.22	4.05	2.54	0.03	1.27	0	0.10	26.83	0	0	101.33
Mine IV	LK-183.08	tt	25.15	3.06	39.00	3.99	2.85	0.05	1.23	0	0.08	26.18	0	0	101.59
Parisit-Fst.	LK-195	tt	25.03	0.97	36.39	6.54	3.39	0.03	2.42	0.17	0.11	25.48	0	0	100.53
Roti Brunnini	LK-201	tt	26.68	0.43	39.81	7.14	7.68	0.06	0.35	0	0.11	18.50	0	0	100.76
Mine I	LK-180.04	(Fe, Ni)AsS	20.69	15.30	0.26	0	44.53	0.19	0	0	0	0	0	Ni: 19.73	100.70

Table A1 (continued).

Sample locality	Sample-#	Mineral	S	Fe	Cu	Zn	As	Se	Ag	Cd	Sn	Sb	Te	Pb	Total
Hohsandhorn	LK-117	gn	13.96	n.a.	0	n.a.	n.a.	0	0.12	0	0	0.13	0.03	84.59	98.83
Hohsandhorn	LK-117	gn	13.96	n.a.	0	n.a.	n.a.	0.02	0.14	0.02	0	0.13	0.06	85.66	99.99
Hohsandhorn	LK-117	gn	13.96	n.a.	0.02	n.a.	n.a.	0.01	0.07	0	0	0.08	0.05	85.91	100.10
Mine I	LK-151	gn	13.47	n.a.	0	n.a.	n.a.	0	0	0.03	0.06	0.19	0	86.24	99.99
Mine I	LK-161	gn	13.96	n.a.	0	n.a.	n.a.	0	0.06	0	0	0.07	0.03	85.45	99.57
Mine I	LK-180.04-3	gn	13.34	n.a.	0.04	n.a.	n.a.	0	0.09	0	0	0.09	0.04	85.53	99.13
Mine I	LK-180.04-3	gn	13.48	n.a.	0	n.a.	n.a.	0	0.08	0.02	0	0.17	0.05	86.40	100.20
Mine I	LK-180.05	gn	13.96	n.a.	0.10	n.a.	n.a.	0	0.08	0.03	0	0.07	0.03	88.32	102.59
Mine I	LK-17/1	gn	13.23	n.a.	0	n.a.	n.a.	0	0.07	0.03	0.05	0.04	0	88.17	101.59
Mine I	LK-184.01	gn	13.07	n.a.	0	n.a.	n.a.	0	0.09	0.02	0.03	0.12	0	85.73	99.06
Mine I	LK-184.01	gn	13.55	n.a.	0	n.a.	n.a.	0	0.04	0.04	0	0.07	0.05	86.11	99.86
Mine II	LK-181.01-1	gn	13.42	n.a.	0	n.a.	n.a.	0	0.09	0.02	0	0.07	0	89.26	102.86
Mine II	LK-181.01-1	gn	13.18	n.a.	0	n.a.	n.a.	0	0.06	0.02	n.a.	0.03	0.09	87.50	100.88
Mine II	LK-181.01-2	gn	12.70	n.a.	0	n.a.	n.a.	0	0.11	0.02	0	0.06	0.05	88.44	101.38
Mine II	LK-181.02	gn	13.25	n.a.	0	n.a.	n.a.	0	0.05	0.03	0	0	0	86.64	99.97
Mine II	LK-181.02	gn	13.34	n.a.	0	n.a.	n.a.	0	0.11	0.02	0	0.11	0.04	85.71	99.33
Mine II	LK-181.01-1	gn	13.96	n.a.	0	n.a.	n.a.	0	0.10	0.02	0	0.09	0.03	86.62	100.82
Mine III	LK-182.09-1	gn	13.47	n.a.	0.05	n.a.	n.a.	0.02	0.11	0.03	0	0.08	0	87.90	101.66
Mine III	LK-182.09-2	gn	13.26	n.a.	0	n.a.	n.a.	0	0.14	0.03	0	0.12	0.03	87.36	100.94
Mine III	LK-182.05	gn	13.02	n.a.	0	n.a.	n.a.	0	0.07	0.04	0.02	0.14	0.04	86.76	100.09
Mine III	LK-182.08	gn	13.96	n.a.	0	n.a.	n.a.	0	0.05	0.02	0.02	0.07	0.04	88.00	102.16
Mine III	LK-17/3	gn	12.88	n.a.	0	n.a.	n.a.	0	0.09	0	0	0.05	0	87.58	100.60
Mine IV	LK-183.01	gn	13.22	n.a.	0.04	n.a.	n.a.	0	0.15	0	0.02	0.11	0.07	87.39	101.00
Mine IV	LK-183.08	gn	13.96	n.a.	0.08	n.a.	n.a.	0	0.10	0.02	0	0.06	0.03	84.75	99.00
Mine IV	LK-183.08	gn	13.96	n.a.	0.15	n.a.	n.a.	0	0.06	0.02	0.04	0.04	0.03	86.84	101.14
Mine IV	LK-183.08	gn	13.96	n.a.	0.14	n.a.	n.a.	0	0.08	0.02	0	0.04	0	84.77	99.01
Mine IV	LK-183.08	gn	13.96	n.a.	0.11	n.a.	n.a.	0	0.03	0	0	0.05	0	86.19	100.34
Mine IV	LK-17/4	gn	13.02	n.a.	0	n.a.	n.a.	0	0.08	0	0	0	0	87.91	101.01
Mines East	LK-138.1	gn	13.96	n.a.	0	n.a.	n.a.	0	0.05	0	0	0.04	0.03	85.66	99.74
Mines East	LK-138.2	gn	13.96	n.a.	0	n.a.	n.a.	0	0.09	0.02	0	0.07	0.03	88.55	102.72
Mines East	LK-138.3	gn	13.96	n.a.	0	n.a.	n.a.	0	0.06	0.03	0	0.07	0.03	88.61	102.76
Mines East	LK-138.1	gn	13.96	n.a.	0	n.a.	n.a.	0	0.09	0.03	0	0.06	0.03	88.58	102.75
Ochsenfeld	LK-2.1	gn	13.28	n.a.	0.03	n.a.	n.a.	0.06	0.28	0.02	n.a.	0	0.06	86.87	100.60
Ochsenfeld	LK-2.1	gn	13.43	n.a.	0	n.a.	n.a.	0.06	0.36	0.02	0	0	0.07	85.65	99.59
Ochsenfeld	LK-2.1	gn	13.96	n.a.	0.03	n.a.	n.a.	0.04	0.31	0.02	0.11	0	0.04	87.93	102.44
Ochsenfeld	LK-2.1	gn	13.24	n.a.	0.03	n.a.	n.a.	0.04	0.27	0.03	n.a.	0	0.08	83.98	97.67
Ochsenfeld	LK-2.2	gn	13.34	n.a.	0	n.a.	n.a.	0.04	0.37	0	0.02	0	0.04	85.88	99.69
Ochsenfeld	LK-2.2	gn	13.27	n.a.	0.06	n.a.	n.a.	0.06	0.33	0.02	0.04	0	0.07	88.99	102.84
Ochsenfeld	LK-2.4	gn	13.24	n.a.	0	n.a.	n.a.	0.05	0.26	0.02	0	0	0.06	84.83	98.46
Ochsenfeld	LK-40.2	gn	13.24	n.a.	0	n.a.	n.a.	0	0.78	0.02	0	0.78	0	85.10	99.92
Ochsenfeld	LK-59	gn	13.45	n.a.	0	n.a.	n.a.	0	0.27	0.04	0	0.29	0	85.65	99.70
Ochsenfeld	LK-188	gn	13.43	n.a.	0	n.a.	n.a.	0	0.19	0.06	0	0.20	0	86.17	100.05
Parisite location	LK-32-1	gn	12.90	n.a.	0	n.a.	n.a.	0	0.18	0.03	0.03	0.16	0.04	87.49	100.83
Parisite location	LK-32-2	gn	12.95	n.a.	0.04	n.a.	n.a.	0	0.27	0.04	0	0.20	0.06	85.26	98.82
Parisite location	LK-32-2	gn	13.02	n.a.	0	n.a.	n.a.	0	0.27	0.04	0	0.16	0.07	89.00	102.56
Parisite location	LK-32-3	gn	12.59	n.a.	0	n.a.	n.a.	0	0.27	0.03	0	0.26	0.04	85.80	98.99
Parisite location	LK-32-4	gn	13.19	n.a.	0.03	n.a.	n.a.	0	0.19	0.04	0	0.19	0	87.29	100.93
Parisite location	LK-32-5	gn	13.19	n.a.	0.13	n.a.	n.a.	0	0.31	0.03	0.08	0.27	0	84.96	98.97
Mine II	LK-63-1	gn incl. in qtz	13.96	n.a.	0	n.a.	n.a.	0	0.10	0	0	0.07	0.08	86.05	100.26

For locality names refer to Figure 2
tn—tennantite
tt—tetrahedrite
gn—galena
gn incl.—galena inclusion (S) in quartz
n.a.—not analysed (galena: Fe, Zn and As were below the detection limit for a few test runs and were not measured in the regular analyses of galena)
zero values—analysed but no signal

Table A2 Single inclusion LA-ICPMS element concentrations (in ppm = µg/g).

LA-ICPMS shot #	sample #	σ	FI-stage	$NaCl_{equiv.}$ [wt%]	Na 23	Mg 25	P 31	K 39	Ca 42	Mn 55	Fe 57	Cu 65	Zn 66	As 75	Rb 85	Sr 88	Ag 107	Sb 121	Cs 133	Ba 137	Pb 208
jr24a04	LK 63-8b	1	A	1.0	2200	n.a.	766	485	2796	< 10	< 119	n.a.	< 12	< 9.2	1.4	1.5	< 2.4	< 3.4	0.5	33	< 1.4
jr24a05	LK 63-8b	1	A	1.0	3674	n.a.	2330	501	< 6568	< 37	< 509	n.a.	< 41	769	< 5.3	3.9	< 7.5	18	< 1.6	< 12	< 5.8
jr24a06	LK 63-8b	1	A	1.0	3504	n.a.	1801	880	< 3272	< 22	< 257	n.a.	< 36	828	< 1.7	< 1.2	< 3.3	< 7.2	< 0.9	19	< 3.2
jr24a07	LK 63-8b	1	A	1.0	3661	n.a.	894	521	< 2227	15	< 162	n.a.	< 16	780	2.9	3.3	< 2.1	15	< 0.5	16	< 2.1
jr24a08	LK 63-8b	1	A	1.0	3623	n.a.	864	417	< 5713	< 41	< 420	n.a.	< 36	1078	< 2.5	2.2	< 9.9	31	< 1.4	24	< 6.0
jr24a09	LK 63-8b	1	A	1.0	2665	n.a.	766	359	< 4359	< 32	< 322	n.a.	< 40	739	< 2.8	< 1.8	< 5.2	17	< 1.4	25	< 3.9
jr24a10	LK 63-8b	1	A	1.0	1178	n.a.	1794	389	4704	49	< 297	n.a.	< 34	246	< 2.6	< 1.9	< 5.3	9.3	< 0.8	< 9.4	< 4.2
jr24a11	LK 63-8b	1	A	1.0	3367	n.a.	1466	747	< 4307	< 31	425	n.a.	35	636	< 2.1	2.3	6.5	15	< 1.2	149	< 3.7
jr24a12	LK 63-8b	1	A	1.0	1970	n.a.	845	144	3468	< 16	< 4507	n.a.	< 18	203	< 1.5	1.0	< 2.7	< 3.5	< 0.6	< 4.1	< 2.3
jr24a13	LK 63-8b	1	A	1.0	2907	n.a.	1082	< 79	1820	< 12	< 151	n.a.	< 22	917	< 0.9	0.7	< 2.1	15	< 0.4	< 3.2	< 1.7
jr24a14	LK 63-8b	1	A	2.0	7267	n.a.	3483	368	< 6484	< 42	807	n.a.	62	265	< 3.4	9.8	< 9.7	20	< 1.9	73	< 7.1
jr24a16	LK 63-8b	1	A	2.0	7071	n.a.	4400	1857	< 15322	< 123	< 1372	n.a.	< 112	343	< 14	< 6.0	< 29	< 40	< 4.8	< 31	< 19
jr23a04	LK 63-11	3	A	0.5	1694	n.a.	< 78	143	< 556	25	191	n.a.	28	65	2.0	2.4	4.8	18	2.8	41	49
jr23a05	LK 63-11	3	A	0.5	1524	n.a.	67	189	266	4.8	466	n.a.	11	34	2.4	1.2	2.9	1.8	0.4	14	13
jr23a07	LK 63-11	3	A	0.5	1724	n.a.	< 38	204	< 299	< 2.0	< 24	n.a.	24	102	0.8	2.7	< 0.5	4.1	1.3	31	18
jr23a08	LK 63-11	3	A	0.5	1457	n.a.	< 29	160	341	3.6	503	n.a.	9.9	58	7.2	4.4	< 0.4	4.5	1.2	70	18
jr23a09	LK 63-11	3	A	0.5	1726	n.a.	< 44	143	< 370	< 2.3	< 28	n.a.	< 4.2	82	5.5	1.5	0.6	5.8	0.9	35	18
jr23a10	LK 63-11	3	A	0.5	1520	n.a.	227	134	< 812	< 5.5	774	n.a.	36	98	< 1.0	3.2	< 1.4	3.2	0.6	43	26
jr23a11	LK 63-11	3	A	0.5	1747	n.a.	< 123	94	< 1142	< 7.3	312	n.a.	< 7.7	102	< 1.2	3.0	9.8	4.1	< 0.5	54	26
jr23a12	LK 63-11	3	A	0.5	1853	n.a.	251	152	< 1290	< 7.9	< 121	n.a.	< 15	97	< 1.8	3.8	< 2.3	< 3.2	0.9	46	20
jr23a13	LK 63-11	3	A	0.5	1742	n.a.	109	197	< 522	< 3.1	81	n.a.	9.2	75	< 0.7	5.5	4.8	3.3	15.1	40	17
jr23a14	LK 63-11	3	A	0.5	1501	n.a.	130	140	< 886	< 5.2	< 63	n.a.	< 7.8	73	1.2	3.0	< 1.7	3.2	< 0.5	50	23
jr23a15	LK 63-11	3	A	0.5	1895	n.a.	< 572	< 201	< 4254	< 24	< 328	n.a.	< 34	137	< 5.6	3.0	< 6.5	< 9.6	< 2.8	55	16
jr23a16	LK 63-11	3	A	0.5	1803	n.a.	< 29	144	< 179	< 1.6	< 16	n.a.	7.5	78	0.5	2.4	< 0.3	3.4	0.7	26	25
jr23a17	LK 63-11	3	A	0.5	1526	n.a.	180	43	< 275	< 1.7	592	n.a.	< 2.8	13	< 0.3	0.6	7.8	10	34	18	20
jr23a18	LK 63-11	3	A	0.5	1600	n.a.		99	< 351	< 2.8	385	n.a.	14	97	1.2	3.1	< 0.7	11	5.0	38	30
	average		A	0.8	2554		1192	355	2233	20	454		24	317	3	3	5	11	5	43	23
jr30a04	LK 63-13-4	3	B	31.73	95987	< 113	< 1197	27519	< 14806	630	1113	< 57	7104	388	65	5095	12	145	219	33098	14892
jr30a05	LK 63-13-4	3	B	31.53	54350	< 2639	< 11334	6747	< 142688	1092	< 9879	< 679	6406	< 937	< 59	2782	< 130	< 352	60	51774	11215
jr30a06	LK 63-13-4	3	B	31.53	51545	< 754	< 5483	6024	73951	761	< 4400	< 238	3777	441	< 26	3103	< 41	216	37	82368	10695
jr30a08	LK 63-13-4	3	B	31.53	71208	< 464	< 2875	13841	< 34958	980	3123	< 181	5329	529	69	4434	< 29	96	78	96508	12236
jr30a09	LK 63-13-4	3	B	31.53	72199	190	< 433	17967	24030	975	2895	< 27	7443	511	47	4997	< 8.3	140	71	79426	13391
jr30a10	LK 63-13-4	3	B	31.20	77699	< 1954	< 9933	16426	< 129055	1265	< 8600	< 421	6326	< 910	< 46	4341	< 126	< 307	40	106692	13774
jr30b04	LK 63-13-5	3	B	31.29	63393	192	< 582	12291	25082	862	2456	< 36	8015	449	49	5025	< 6.0	115	62	109332	15100
jr30b05	LK 63-13-5	3	B	31.43	45825	< 1209	< 5169	6640	75819	424	< 4428	< 230	4075	360	41	3321	< 80	204	27	93758	9207
jr30b06	LK 63-13-5	3	B	31.48	71540	< 1695	9724	12888	< 99054	< 618	5196	< 394	8775	< 585	< 25	4950	< 120	< 239	101	105961	14890
jr30b08	LK 63-13-5	3	B	31.85	58762	< 907	< 6481	12689	< 70262	864	5647	< 296	10093	865	< 48	3652	< 74	< 231	74	81983	15440
jl04a04	LK 63-12b	3	B	31.50	84204	148	1160	18210	< 23537	890	3470	< 78	7037	543	56	5354	< 23	129	106	73311	12684
jl04a05	LK 63-12b	3	B	31.50	72208	142	485	13262	24274	965	3135	21	6051	446	48	5222	< 4.5	121	71	96188	11354
jl04a06	LK 63-12b	3	B	31.50	66455	273	< 1982	9918	< 34341	1103	< 1748	81	6452	243	23	5713	< 28	109	43	130570	13878
jl04a07	LK 63-12b	3	B	31.50	95544	< 1654	< 5028	31388	< 68433	286	< 4662	< 299	3738	357	136	8316	< 60	< 71	361	37864	18182
jl04a08	LK 63-12b	3	B	31.50	80783	405	646	15698	16414	793	1916	412	4848	487	64	3800	45	156	106	82344	9620

Table A2 (continued).

LA-ICPMS shot #	sample #	σ	FI-stage	$NaCl_{equiv.}$ [wt%]	Na 23	Mg 25	P 31	K 39	Ca 42	Mn 55	Fe 57	Cu 65	Zn 66	As 75	Rb 85	Sr 88	Ag 107	Sb 121	Cs 133	Ba 137	Pb 208
jl04a09	LK 63-12b	3	B	31.50	70477	< 192	< 1533	16434	29021	992	3450	< 69	5732	560	49	4446	< 30	96	95	88941	11217
jl04a10	LK 63-12b	3	B	31.50	82037	< 283	3805	21050	< 41756	1075	3172	< 119	8558	735	52	5206	< 54	201	104	81508	14648
jl04a11	LK 63-12b	3	B	31.50	52872	< 621	5354	1776	< 77013	1801	4950	< 244	794	926	< 22	850	< 89	321	25	171105	8036
jl04a12	LK 63-12b	3	B	31.50	65919	225	815	13570	29114	836	2865	< 40	6198	349	55	4477	< 10	87	69	107271	12907
jl04a13	LK 63-12b	3	B	31.50	64673	< 416	< 1978	13732	< 33880	1332	3506	< 127	6795	407	29	5277	< 31	117	76	123228	11420
	average		B	31.51	69884	225	3141	14403	37213	944	3350	172	6177	506	56	4518	28	150	91	91661	12739
jr30b07	LK 63-13-5	3	BC1	28.0	47814	< 590	4918	9176	48141	971	3305	< 112	6104	843	63	4312	< 34	180	69	81935	11304
jr23e07	LK 63-13-5	1	BC2	7.3	6509	n.a.	20909	< 3247	< 49916	< 318	< 5785	n.a.	< 837	< 512	136	126	< 110	< 111	< 26	1998	242
jr23e06	LK 63-13-4	1	BC2	6.5	13234	n.a.	91551	12192	< 160204	< 911	< 12209	n.a.	3504	< 1593	< 191	1231	< 368	796	< 69	17517	4181
jr23e08	LK 63-13-5	1	BC2	5.0	5430	n.a.	4543	< 671	24609	< 66	< 922	n.a.	< 187	332	14	64	< 17	62	5.4	1500	205
jr23e09	LK 63-13-5	1	BC2	5.0	13960	n.a.	< 2022	1111	< 12790	104	2208	n.a.	< 196	< 124	< 14	323	< 25	107	11	4053	908
jr23c04	LK 63-13-3	1	C	1.9	1859	n.a.	< 1202	< 481	10281	< 60	< 830	n.a.	< 65	132	< 7.8	3.8	< 18	< 21	< 3.8	< 17	14
jr23c06	LK 63-13-3	1	C	1.9	2818	n.a.	2525	921	7487	< 39	< 450	n.a.	< 51	< 43	< 7.1	< 2.3	7.0	< 9.8	< 3.2	176	< 6.5
jr23c07	LK 63-13-3	1	C	1.9	4480	n.a.	< 812	1576	< 5792	438	434	n.a.	< 51	193	< 5.4	4.6	14	105	8.2	104	< 7.3
jr23c08	LK 63-8a	1	C	1.9	6462	n.a.	1819	721	< 3537	< 23	967	n.a.	80	84	< 3.5	45	29	< 5.5	13	831	113
jr23c09	LK 63-8a	1	C	1.9	7115	n.a.	< 1418	< 489	< 9450	< 62	< 931	n.a.	< 93	330	< 9.0	14	21	< 21	14	623	94
jr23c10	LK 63-8a	1	C	1.9	3766	n.a.	< 1221	< 405	< 7302	164	1351	n.a.	258	259	< 7.7	24	< 12	569	15	601	104
jr23c11	LK 63-8a	1	C	1.9	6154	n.a.	3015	< 682	< 10567	< 79	< 831	n.a.	< 134	132	< 11	32	< 19	< 21	325	2142	164
jr23c12	LK 63-8a	1	C	1.9	4490	n.a.	3242	< 365	< 7145	< 45	< 547	n.a.	< 52	236	< 8.1	9.5	< 16	< 15	6.7	507	66
jr23c13	LK 63-8a	1	C	1.8	6523	n.a.	299	153	913	7	< 60	n.a.	< 7.1	268	< 0.6	0.4	1.5	9.5	75	< 1.9	< 1.0
jr23c14	LK 63-8a	1	C	1.8	7011	n.a.	< 3142	< 1237	< 26798	< 178	< 2209	n.a.	< 191	942	< 23	< 14	< 48	< 48	< 10	58	< 28
jr23c15	LK 63-8a	1	C	1.8	6753	n.a.	2050	870	< 75286	< 54	< 658	n.a.	< 83	738	< 7.3	5.4	< 12	409	6.0	< 15	< 8.2
jr23c16	LK 63-8a	1	C	1.8	6651	n.a.	1748	1104	< 5152	< 33	< 386	n.a.	< 56	810	< 4.5	2.4	< 9.0	< 11	< 2.0	< 10	< 6.0
jr23d07	LK 63-13-2	1	C	1.1	3769	n.a.	4449	< 480	< 8999	< 55	< 637	n.a.	< 64	< 76	< 9.4	< 2.7	< 22	< 16	< 4.1	< 14	< 10
jr23d08	LK 63-13-2	1	C	1.1	3980	n.a.	< 1215	< 463	< 8560	< 58	< 756	n.a.	93	< 72	22	< 3.9	< 18	36	7.3	< 15	49
jr23d09	LK 63-13-2	1	C	1.1	3723	n.a.	9551	< 1015	< 16806	135	< 1272	n.a.	< 203	< 119	< 15	< 6.3	< 41	< 35	< 7.7	< 41	< 21
jr23d10	LK 63-13-2	1	C	1.1	3241	n.a.	2143	954	< 9078	< 53	1115	n.a.	< 117	135	< 8.2	< 5.4	< 14	25	< 4.7	< 21	21
jr23d12	LK 63-13-1	1	C	1.2	2640	n.a.	< 340	1157	< 2569	< 17	294	n.a.	< 38	44	< 3.4	2.8	< 5.6	< 6.9	< 1.5	< 4.5	< 2.8
jr23e04	LK 63-13-1	1	C	1.2	4692	n.a.	4125	< 360	< 6979	< 38	< 517	n.a.	< 70	187	< 4.2	< 2.0	< 10	21	7.3	77	24
jr23e05	LK 63-13-1	1	C	1.2	4392	n.a.	< 1298	< 427	< 8005	< 44	600	n.a.	< 89	< 65	< 8.1	< 2.8	< 14	< 16	22	< 18	28
jr23d11	LK 63-13-1	1	C	1.2	3895	n.a.	< 669	395	< 4746	< 30	925	n.a.	< 43	64	< 5.3	3.0	< 7.9	14	< 2.9	< 10	28
	average		C	1.6	4721		3179	872	6227	186	812		144	304	22	12	14	149	45	569	64

The number below the element abbreviation represents the measured isotope
σ—Standard deviations of the background applied for significancy of LA-ICPMS signals (Longerich et al., 1996)
$NaCl_{equiv.}$ —derived from microthermometry using equations of Bodnar and Vityk (1994) and Diamond (1992)